

## A SURVEY OF H I 21 CENTIMETER EMISSION LINES TOWARD SUPERNOVA REMNANTS

BON-CHUL KOO<sup>1</sup> AND CARL HEILES

Astronomy Department, University of California, Berkeley, CA 94720

Received 1991 February 19; accepted 1991 May 31

## ABSTRACT

We performed a survey of H I 21 cm emission lines toward all known northern supernova remnants (SNRs) in order to find rapidly expanding SNR shells. Among 103 sources we detected 15 SNRs that have associated high-velocity H I gas, most of which are quite likely the gas accelerated by the supernova (SN) blast wave. The velocity of H I gas in 15 sources ranges from 70 to 160 km s<sup>-1</sup> with respect to their systematic velocities, and the dynamic age ranges from 3 × 10<sup>4</sup> to 5 × 10<sup>5</sup> yr with most (80%) of them younger than 1.2 × 10<sup>5</sup> yr. In four sources, G27.7–0.6, W51, CTB 80, and HB 21, the velocity structure implies that the high-velocity gas is a portion of an expanding shell. We obtained the mass per unit line-of-sight velocity  $v_\ell$  interval in these four sources, and it varies as  $M(v_\ell) \propto v_\ell^{-3}$ . This mass distribution may reflect the characteristics of the general interstellar medium, i.e., multiphase interstellar medium. The 15 sources are individually discussed. We also detected 12 SNRs that possibly have associated H I shells. These 12 sources show an excess H I emission significantly brighter than the surrounding region over a wide (>10 km s<sup>-1</sup>) velocity interval, which is very likely to be associated with SNRs.

*Subject headings:* interstellar: matter — nebulae: supernova remnants — radio sources: 21 cm radiation

## 1. INTRODUCTION

In his classic paper, Woltjer (1972) divided the evolution of supernova remnants (SNRs) in a uniform medium into four phases: (1) the free expansion phase, in which the inertia of the swept-up mass is negligible and the stellar ejecta freely expands; (2) the energy-conserving phase or Sedov phase, in which the ambient gas is swept up by the energy-conserving blast wave; (3) the momentum-conserving phase or snowplow phase, where the swept-up ambient gas radiatively cools to form a dense neutral shell and the shell sweeps out the ambient gas; and finally (4) the merging phase, in which the SNR slows down to a velocity comparable to the random velocity of the interstellar medium and loses its identity. This simple picture has worked and still remains a useful guide for describing the evolution of SNRs. During the last two decades, especially with the development of numerical techniques, our understanding on the dynamical evolution of SNRs has been improved, and we have a good theoretical estimate of when the shell formation occurs for SNRs evolving in a uniform medium.

For hydrogen density  $n_0 = 1 \text{ cm}^{-3}$ , for example, the shell formation occurs at  $t_{\text{sf}} \approx 36,000 \text{ yr}$  at which time the shell radius is 20 pc and the velocity is 180 km s<sup>-1</sup> (Cioffi, McKee, & Bertschinger 1989). The shell cools rapidly, and is driven by the thermal pressure of the hot gas inside; this is called the “pressure-driven snowplow phase” (Chevalier 1974; McKee & Ostriker 1977). For SNRs older than the shell-formation time  $t_{\text{sf}}$ , therefore, we expect to observe fast-expanding SNR shells in the H I 21 cm line. If the H I line is optically thin, the line profile will be either two separate narrow peaks or a wide rectangular shape, depending on whether the source is resolved by the telescope beam or not. It is the purpose of this paper to detect H I shells in old SNRs.

Observationally, it is very difficult to detect expanding H I

shells, because most known SNRs are located in the Galactic plane where the Galactic background H I emission causes severe contamination. There have been papers reporting the detection of H I shells associated with SNRs, but most of these shells have expansion velocities smaller than  $\sim 20 \text{ km s}^{-1}$ , which is not enough for a H I shell to be clearly discernible from the background emission (Assoua & Erkes 1973; Knapp & Kerr 1974; Colomb & Dubner 1980, 1982). High-velocity H I gas has been detected in G78.2+2.1, CTB 109, and VRO 42.05.01, but no shell structure is obvious (Landecker, Roger, & Higgs 1980; Braun & Strom 1986). Probably the two most reliable detections are for IC 443 (DeNoyer 1978; Giovanelli & Haynes 1979; Braun & Strom 1986) and for CTB 80 (Koo et al. 1990). For IC 443, the approaching portion of a partially complete H I shell has been clearly seen in the channel maps by Braun and Strom. For CTB 80, Koo et al. detected the receding portion of a partially complete H I shell expanding at  $\sim 72 \text{ km s}^{-1}$ .

H I shells, if they are found, provide estimates for important SNR-related parameters: the size, expansion velocity, mass, and kinetic energy of the shell, from which we can derive the age of the SNR and the initial explosion energy of the SN based on some assumptions. A probably more important aspect, however, is that the H I shells may tell us how SNRs evolve in *real* circumstances: The ambient medium that SNRs evolve into seems to be neither uniform nor homogeneous. The interstellar medium is known to be composed of at least three components with largely different densities (McKee & Ostriker 1977; Shull 1987). Observationally, we have many examples suggesting that an individual SNR interacts with several components of the interstellar medium. For example, the radio map of VRO 42.05.01 strongly suggests that it has crossed a rarefied region, which may be a tunnel filled with hot gas (Pineault, Landecker, & Routledge 1987). Many other SNRs have partially complete radio shells. Also, the fact that two expanding H I shells in IC 443 and CTB 80 are not complete implies an inhomogeneous ambient medium.

There have not been many theoretical studies on the evolu-

<sup>1</sup> Postal address: Harvard-Smithsonian Center for Astrophysics, 60 Garden Street, Cambridge, MA 02138.

tion of SNRs in a multiphase interstellar medium (see review by McKee 1988). Furthermore, some Type II (and Type Ib) supernovae should explode inside a bubble blown out by the progenitor star, or inside a cavity formed by a previous supernova located in the same stellar cluster or association. In this case, the SNR expands almost freely until the shock hits the preexisting dense shells, and then the evolution slowly approaches that of a standard model (Chevalier & Laing 1989; Tenorio-Tagle et al. 1990). Therefore, the ambient medium with which SNRs interact seems to be far from the idealized uniform medium, and the observational study of large, old SNRs might be helpful both in revealing the structure of the interstellar medium and in understanding the theory of the realistic case.

We performed a sensitive H I 21 cm survey of 103 SNRs—all SNRs in the catalog of Green (1988) available to our telescope at Hat Creek Radio Observatory—to search for H I shells in SNRs. We detected 15 SNRs that have associated high-velocity H I gas, most of which are quite likely the gas accelerated by the SN blast wave. We also detected 12 SNRs that possibly have associated H I shells. The observational procedures are summarized in § 2, and the results of the survey are given in § 3. The physical parameters of the 15 SNRs with associated high-velocity H I gas are derived in § 4.1. There is no apparent correlation among physical parameters, and the implication is discussed in § 4.2. Among 15 SNRs, four sources show a velocity structure implying an expanding shell. The mass per unit line-of-sight velocity interval is derived for these four sources and is discussed in § 4.3. The individual sources are briefly discussed in § 4.4, and the results are summarized in § 5.

## 2. OBSERVATIONS AND DATA ANALYSIS

We used the 85 foot (26 m) telescope of the Hat Creek Radio Observatory during 1989 and 1990. We first observed each SNR at nine points in a cross pattern centered at its catalog position. The cross pattern was aligned along the north-south and east-west directions, and each point was separated by a full beamwidth (36') from its neighbor point. The central position was observed twice, at the beginning and at the end of the cycle, in order to monitor any unusual change of observational conditions during a cycle. We observed both circular polarizations simultaneously with two 512 channel correlators, each with a total bandwidth of 5 MHz, so that the total velocity coverage was  $1060 \text{ km s}^{-1}$  and the velocity resolution was  $4.1 \text{ km s}^{-1}$  (after Hanning smoothing). We frequency-switched to higher frequencies by 5 MHz and integrated 400 s, so that a typical rms noise level is about 0.04 K. We present our results in antenna temperature; the main-beam brightness temperature can be obtained by dividing the antenna temperature by  $\eta_b \approx 0.80$ .

We used the nine profiles to determine the velocities at which a SNR exhibits excess, if any, H I over the background. We divided SNRs into four ranks, in which increasing number implies increasing reliability of a detected H I shell:

Rank 1: The H I line at the center has excess emission wider than  $10 \text{ km s}^{-1}$  and brighter than the four outermost positions.

Rank 2: Same as rank 1, but the excess emission is brighter than all eight outer positions.

Rank 3: Same as rank 2, but the excess emission occurs at an extreme positive or negative velocity.

All other sources are ranked 0.

We want to emphasize that we are looking for fast-expanding

SNR shells which appear as an excess emission over the background emission, not H I holes that would be present at the systematic velocity of SNRs. With our sensitivity of  $\sim 0.06 \text{ K}$  ( $1.5 \sigma$ ), the minimum detectable H I mass inside the  $10 \text{ km s}^{-1}$  velocity interval is  $\sim 1.3d^2 M_\odot$  by assuming that the source is unresolved, where  $d$  is the distance to the source in kiloparsecs. Note that this sensitivity is enough to detect most SNR shells, because if an old SNR shell is expanding at  $v_{\text{exp}}$  in an idealized uniform medium of hydrogen density  $n_0$ , then the H I mass per unit line-of-sight velocity is  $M_{\text{HI}}/(2v_{\text{exp}}) \sim 2.2(R/20 \text{ pc})^{5.3} n_0^{1.9} M_\odot/(\text{km s}^{-1})$  where  $R$  is the radius of the SNR (cf. eq. [2]). SNRs ranked 3 have very high velocity H I gas confined to the center. Such gas is rare; thus it is very probable that the gas is really associated with the SNR. SNRs ranked 2 have excess H I gas confined to the position of SNRs, but not at an extreme velocity. Real association with the SNR is less certain, but the positional coincidence is highly suggestive. We regard the rank 1 classification as having a high probability of being a random fluctuation.

Supernova remnants are radio continuum sources, and as such present a background source against which the H I can produce absorption instead of emission. Such absorption may prevent the detection of the approaching portion of a SNR shell if the brightness temperature of the continuum emission  $T_B$  is stronger than the spin temperature. (We say brightness temperature instead of antenna temperature because we assume the SNR shell size to be comparable to the radio continuum size.) In most SNR shells, the density is probably high enough,  $n_0 > (T_B/2400 \text{ K})$ , for the spin temperature to be equal to the gas kinetic temperature  $T_k$ . [The above expression follows from  $n_0 \gamma_{21} > (kT_B/h\nu)A_{21}$ , where the collisional de-excitation rate  $\gamma_{21} \sim 1 \times 10^{-10} \text{ cm}^3 \text{ s}^{-1}$  between  $T_k = 30$  and  $1000 \text{ K}$ ; Spitzer 1978.] The kinetic temperature of H I gas is not likely to be much lower than  $100 \text{ K}$ . Then, since the old SNRs with associated dense neutral shells have presumably weak continuum emission (see § 3.2), it is not likely that the H I emission from a SNR shell is significantly affected by the continuum emission in most cases.

Figure 1 shows a sample spectrum of each rank. In Figure 1 the thick solid line is the spectrum at the center, the dotted line is the excess emission brighter than the four outermost off-center positions, and the thin solid line is the excess emission brighter than all eight off-center positions.

The ranking of SNRs in this way is useful for a preliminary classification. However, it is clear that we cannot reach any firm conclusion based solely on the above observations. In fact, it turned out that some SNRs were ranked 3 because of the relative angle of our cross pattern to the Galactic plane. Therefore, after assigning a rank to each SNR, we made small maps for all sources ranked 2 or 3 except for G0.9+0.1, which is located near the Galactic center. The size of maps is  $9 \times 9$  points at half-beam spacing, and the velocity resolution was  $2.1 \text{ km s}^{-1}$  (after Hanning smoothing).

## 3. RESULTS

### 3.1. Catalogs and Maps

The results of our survey are summarized in Table 1. Source parameters are from Green (1988), except for the angular size G69.0+2.7 (CTB 80). For CTB 80, we adopt  $64'$ , which is the angular diameter of an infrared shell detected by Fesen, Shull, & Saken (1988). For all other SNRs, the size is the angular size in radio continuum; a single value is quoted for nearly circular

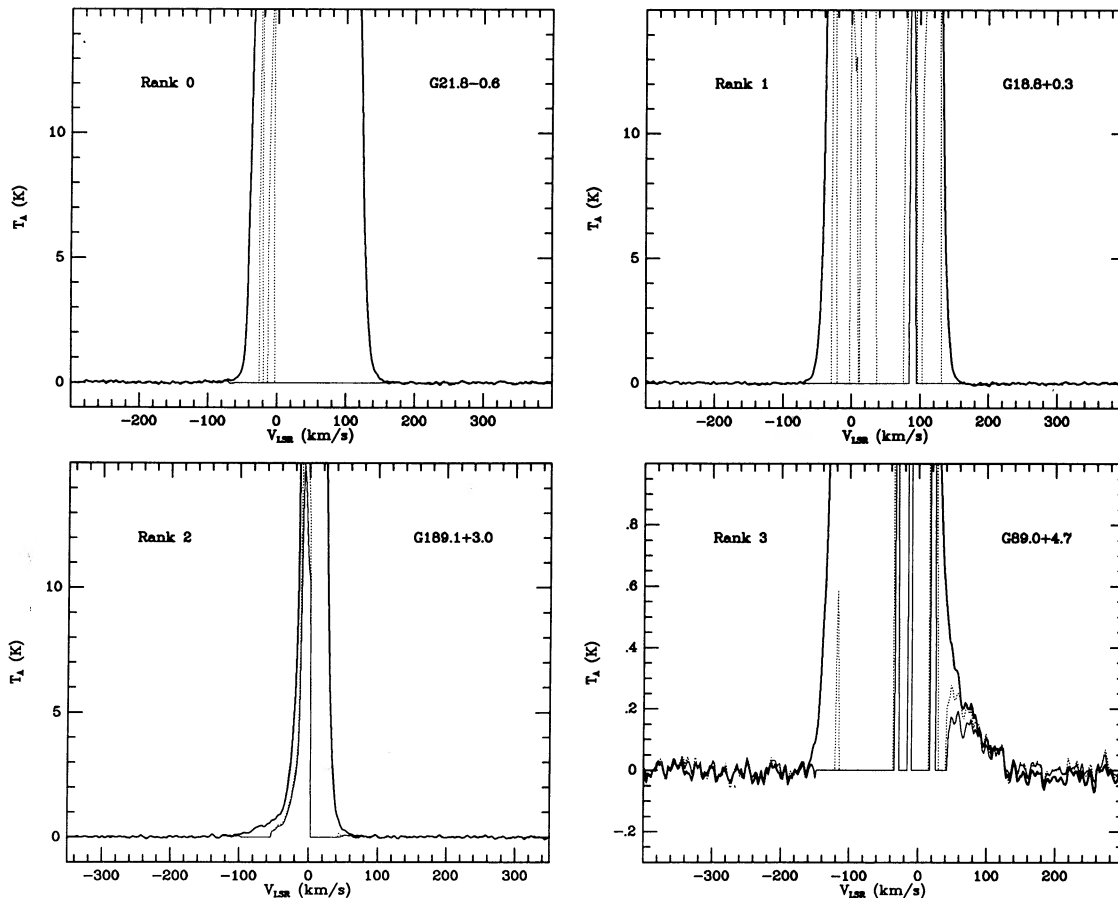


FIG. 1.—Sample H I spectra of four different ranks. The thick solid line is the spectrum at the center, the dotted line is the excess emission brighter than the four outermost off-center positions, and the thin solid line is the excess emission brighter than all eight off-center positions. The probability of a real association of the excess emission with a SNR is very high for rank 3 and decreases to very low for rank 0 (see text).

remnants, and the product of two values, the major and minor axes, is quoted for elongated remnants. The type, “S,” “F,” or “C,” represents SNRs with a “shell,” “filled-center,” or “composite” radio structure, respectively. The uncertain parameters are listed with a question mark.

Among 103 sources, 20 SNRs are ranked 3, 25 SNRs are ranked 2, 19 SNRs are ranked 1, and 39 SNRs are ranked 0. As we already know from Koo et al. (1990), CTB 80 is ranked 3. However, IC 443, the other SNR with a probable expanding H I shell, is ranked 2 because there is high-velocity H I gas in the surrounding medium.

As mentioned in the previous section, we made small maps for all sources ranked 2 or 3 except for G0.9+0.1. We first made maps of  $10.3 \text{ km s}^{-1}$  velocity intervals, and visually inspected them for evidence for expanding H I shells.

The maps of most rank 2 sources show nothing evident visually. Some rank 2 sources, however, show an excess emission within a wide velocity interval, which is possibly associated with SNRs. In order to select those sources objectively, we compared the average brightness of the region with radius 1.5 times larger than the remnant radius with that of the surrounding pixels. The comparison was performed at  $2.1 \text{ km s}^{-1}$  velocity intervals over the velocity range where the excess emission appeared in our cross-pattern survey. Table 2 lists each velocity interval in which the average brightness is greater than that of the surrounding pixels by more than their rms fluctuation, and the average *excess* integrated antenna temperature in that

velocity interval. This criterion has picked most of the suspicious features. There were, however, several features with relatively strong peaks at the SNRs and with average brightnesses greater than those of the surrounding pixels, but they were not selected because the difference is smaller than the rms fluctuation. We included these emission features in Table 2 in parentheses.

The excess emissions listed in Table 2 are possibly associated with SNRs. In particular, 12 sources G6.4–0.1 (W28), G8.7–0.1 (W30), G11.4–0.1, G12.0–0.1, G32.8–0.1 (Kes 78), G33.6+0.1 (HC 13), G39.2–0.3 (HC 24), G93.7–0.2 (CTB 104A), G189.1+3.0 (IC 443), C349.7+0.2, G352.7–0.1, and G357.7–0.1 (MSH 17–39) have excess emissions in the velocity range wider than  $10 \text{ km s}^{-1}$ , which are very likely to be associated with SNRs; IC 443 falls in this category. However, since we are sampling all the gas along a line of sight, we cannot be sure of the association just based on our observations. In order to confirm the possibility, high-resolution H I maps might be helpful, which can be used to study the velocity structure and can be compared with radio continuum maps. In Figure 2 we show maps of integrated antenna temperature of rank 2 sources with wide excess emissions ( $\geq 10 \text{ km s}^{-1}$ ), which might be useful for further studies.

All rank 3 sources show some high-velocity excess emissions near SNRs. Table 3 lists the velocity range within which excess emission appears,  $v_{\min}$  and  $v_{\max}$ , which is defined by the excess antenna temperature being larger than  $0.06 \text{ K}$  ( $1.5 \sigma$ ) in our

TABLE 1  
SUMMARY OF SURVEY RESULTS

Galactic Coordinates	Name(s)	$\alpha$ (1950)	$\delta$ (1950)	Size (arcmin)	Type	Flux at 1 GHz (Jy)	Rank
0.9+0.1	...	17 <sup>h</sup> 44 <sup>m</sup> 12 <sup>s</sup>	-28°08'	8	C	18?	2
1.9+0.3	...	17 45 37	-27 09	1.2	S	0.6	0
4.5+6.8	Kepler, SN 1604, 3C 358	17 27 42	-21 27	3	S	19	1
5.4-1.2	Milne 56	17 59 00	-24 55	35	C?	35?	1
5.9+3.1	...	17 44 20	-22 15	20	S	3.3?	0
6.4-0.1	W28	17 57 30	-23 25	42	C	310	2
6.4+4.0	...	17 42 10	-21 20	31	S	1.3?	0
7.7-3.7	...	18 14 20	-24 05	18	S	10	2
8.7-0.1	(W30)	18 02 35	-21 25	45	S?	90	2
9.8+0.6	...	18 02 10	-20 14	12	S	3.9	3
10.0-0.3	...	18 05 40	-20 26	8?	S?	2.9	2
11.2-0.3	...	18 08 30	-19 26	4	S	22	0
11.4-0.1	...	18 07 50	-19 06	8	S?	6	2
12.0-0.1	...	18 09 15	-18 38	5?	?	3.5	2
15.9+0.2	...	18 16 00	-15 03	7 × 5	S?	4.5?	1
16.8-1.1	...	18 22 30	-14 48	30 × 24?	?	2?	0
18.8+0.3	Kes 67	18 21 10	-12 25	18 × 13	S	27	1
18.9-1.1	...	18 27 00	-13 00	33	C?	37	0
20.0-0.2	...	18 25 20	-11 37	10	F	10	2
21.5-0.9	...	18 30 37	-10 37	1.2	F	6	0
21.8-0.6	Kes 69	18 30 00	-10 10	20	S	69	0
22.7-0.2	...	18 30 30	-09 15	26	S?	33	3
23.3-0.3	W41	18 32 00	-08 50	27	S	70	2
23.6+0.3	...	18 30 20	-08 15	10?	?	8?	1
24.7-0.6	...	18 36 00	-07 35	15?	S?	8	3
24.7+0.6	...	18 31 30	-07 07	30 × 15	C?	20?	1
27.4+0.0	4C-04.71	18 38 40	-04 59	4	S	6	2
27.8+0.6	...	18 37 06	-04 28	50 × 30	F	30	0
29.7-0.3	Kes 75	18 43 48	-03 02	3	C?	10	2
30.7+1.0	...	18 42 10	-01 35	24 × 18	S?	6	1
31.5-0.6	...	18 48 35	-01 35	18?	S?	2?	0
31.9+0.0	3C 391	18 46 50	-00 59	5	S	24	1
32.0-4.9	3C 396.1	19 03 00	-03 00	60?	S?	22?	0
32.8-0.1	Kes 78	18 48 50	-00 12	17	S?	11?	2
33.2-0.6	...	18 51 12	-00 05	18	S	5?	0
33.6+0.1	Kes 79, 4C 00.70, HC 13	18 50 15	+00 37	10	S	22	2
34.7-0.4	W44, 3C 392	18 53 30	+01 18	35 × 27	S	230	3
36.6-0.7	...	18 58 05	+02 52	25?	S?	?	0
39.2-0.3	3C 396, HC 24, NRAO 593	19 01 40	+05 23	8 × 6	S	18	2
39.7-2.0	W50, SS 433	19 10 00	+04 50	120 × 60	?	85?	3
40.5-0.5	Flo	19 04 45	+06 26	22	S	11	3
41.1-0.3	3C 397	19 05 08	+07 03	4.5 × 2.5	S	22	3
42.8+0.6	...	19 04 55	+09 00	24	S	3?	3
43.3-0.2	W49B	19 08 44	+09 01	4 × 3	S	38	1
45.7-0.4	...	19 14 05	+11 04	22	S	4.2	0
46.8-0.3	(HC 30)	19 15 50	+12 04	17 × 13	S	14	1
49.2-0.7	(W51)	19 21 30	+14 00	25?	S?	160?	3
53.6-2.2	3C 400.2, NRAO 611	19 36 30	+17 08	28	S	8	0
54.1+0.3	...	19 28 28	+18 46	1.5	F?	0.5	1
54.4-0.3	(HC 40)	19 31 10	+18 50	40	S	28	3
55.7+3.4	...	19 19 10	+21 38	23	S	1.4	0
57.2+0.8	(4C 21.53)	19 32 50	+21 50	12?	S?	1.8?	0
65.3+5.7	...	19 31 00	+31 05	310 × 240	S?	52?	3
65.7+1.2	DA 495	19 50 10	+29 18	18	F?	5.1	2
69.0+2.7	CTB 80	19 51 30	+32 45	64	?	120?	3
73.9+0.9	...	20 12 20	+36 03	22?	S?	9?	0
74.0-8.5	Cygnus Loop	20 49 00	+30 30	230 × 160	S	210	0
74.9+1.2	CTB 87	20 14 10	+37 03	8 × 6	F	9	0
78.2+2.1	DR 4, $\gamma$ Cygni	20 19 00	+40 15	60	S	340	3
82.2+5.3	W63	20 17 30	+45 20	95 × 65	S	120?	0
84.2-0.8	...	20 51 30	+43 16	20 × 16	S	11	1
89.0+4.7	HB 21	20 43 30	+50 25	120 × 90	S	220	3
93.3+6.9	DA 530, 4C(T) 55.38.1	20 51 00	+55 10	27 × 20	S	9	0
93.7-0.2	CTB 104A, DA 551	21 27 45	+50 35	80	S	65	2
94.0+1.0	3C 434.1	21 23 10	+51 40	30 × 25	S	15	1
109.1-1.0	CTB 109	22 59 30	+58 37	28	S	20	0
111.7-2.1	Cassiopeia A, 3C 461	23 21 10	+58 32	5	S	2720	0
112.0+1.2	...	23 13 40	+61 30	30?	S?	7?	1
114.3+0.3	...	23 34 45	+61 38	90 × 55	S	6?	0

TABLE 1—Continued

Galactic Coordinates	Name(s)	$\alpha(1950)$	$\delta(1950)$	Size (arcmin)	Type	Flux at 1 GHz (Jy)	Rank
116.5+1.1.....	...	23 51 20	+62 58	80 × 60	S	11?	0
116.9+0.2.....	CTB 1	23 56 40	+62 10	34	S	9?	3
117.4+5.0.....	...	23 52 30	+67 30	60 × 80?	S?	30?	3
119.5+10.2.....	CTA 1	00 04 00	+72 30	90	S	36	3
120.1+1.4.....	Tycho, 3C 10, SN 1572	00 22 30	+63 52	8	S	56	0
126.2+1.6.....	...	01 18 30	+64 00	70	S?	7	1
127.1+0.5.....	R5	01 25 00	+62 55	45	S	13	0
130.7+3.1.....	3C 58, SN 1181	02 01 55	+64 35	9 × 5	F	33	0
132.7+1.3.....	HB 3	02 14 00	+62 30	80	S	45	0
152.2-1.2.....	...	04 05 30	+48 24	110?	S?	16?	0
160.9+2.6.....	HB 9	04 57 00	+46 36	140 × 120	S	110	0
166.0+4.3.....	VRO 42.05.01	05 23 00	+42 52	55 × 35	S	7?	3
166.2+2.5.....	OA 184	05 15 30	+41 50	90 × 70	S	11	3
179.0+2.6.....	...	05 50 30	+31 05	70	S?	7	0
180.0-1.7.....	S147	05 36 00	+27 50	180	S	65	1
184.6-5.8.....	Crab Nebula, 3C 144, SN 1054	05 31 30	+21 59	7 × 5	F	1040	0
189.1+3.0.....	IC 443, 3C 157	06 14 00	+22 36	45	S	160	2
192.8-1.1.....	PKS 0607+17	06 06 30	+17 20	78	S	20?	3
205.5+0.5.....	Monoceros Nebula	06 36 00	+06 30	220	S	160	0
206.9+2.3.....	PKS 0646+06	06 46 00	+06 30	60 × 40	S?	6	0
211.7-1.1.....	...	06 43 10	+00 24	70?	S?	15?	0
240.9-0.9.....	...	07 40 30	-25 06	95?	S?	24?	1
261.9+5.5.....	...	09 02 20	-38 30	40 × 30	S	10?	2
348.5+0.1.....	CTB 37A	17 10 40	-38 29	10	S	72	2
348.7+0.3.....	CTB 37B	17 10 30	-38 08	10	S	26	2
349.7+0.2.....	...	17 14 35	-37 23	2.5 × 2	S?	20	2
350.0-1.8.....	...	17 23 40	-38 20	30?	S?	31	0
350.1-0.3.....	...	17 17 40	-37 24	4?	?	5.6	1
351.2+0.1.....	...	17 19 05	-36 08	7	S	5.8	2
352.7-0.1.....	...	17 24 20	-35 05	6 × 5	S?	6?	2
355.9-2.5.....	...	17 42 35	-33 42	13	S	8	0
357.7-0.1.....	MSH 17-39	17 37 15	-30 56	3 × 8?	?	37	2
357.7+0.3.....	...	17 35 20	-30 42	24	S	10	2
359.1-0.5.....	...	17 42 20	-29 56	24	S	14	1

NOTE.—Source parameters are from Green 1988, except for the angular size of CTB 80, which is taken from Fesen et al. 1988.

TABLE 2  
EXCESS EMISSIONS AT RANK 2 SUPERNOVA REMNANTS

Galactic Coordinates	$v_{\min}, v_{\max}$ (km s <sup>-1</sup> )	$\int \Delta \bar{T}_A dv$ (K km s <sup>-1</sup> )	Notes	Galactic Coordinates	$v_{\min}, v_{\max}$ (km s <sup>-1</sup> )	$\int \Delta \bar{T}_A dv$ (K km s <sup>-1</sup> )	Notes
0.9+0.1.....	...	...	1	32.8-0.1.....	+75.3, +93.8	110 ± 60	
6.4-0.1.....	-5.7, +2.5	64 ± 50	2	33.6+0.1.....	+48.0, +54.1	40 ± 30	
	(+97.4, +113.9)	(20 ± 42)			+63.4, +69.6	41 ± 24	
	+131.5, +141.8	30 ± 31			+88.2, +115.0	150 ± 110	
7.7-3.7.....	+64.8, +70.9	1.1 ± 0.8		39.2-0.3.....	+74.3, +86.6	55 ± 24	
8.7-0.1.....	+2.6, +4.6	12 ± 12	2	65.7+1.2.....	+36.0, +44.2	6.3 ± 5.3	
	+43.8, +50.0	50 ± 47		93.7-0.2.....	(-139.7, -129.4)	(0.7 ± 1.5)	2
	(+111.9, +126.3)	(33 ± 51)			-37.6, -33.5	26 ± 25	
10.0-0.3.....	-6.7, +1.5	39 ± 22		189.1+3.0.....	-47.4, -14.5	15 ± 14	3
	+73.7, +79.9	12 ± 7		261.9+5.5.....	+98.5, +106.7	2.9 ± 2.5	
	+155.2, +157.2	3.6 ± 3.6		348.5+0.1.....	-50.0, -41.8	16 ± 13	4
11.4-0.1.....	+11.9, +28.3	71 ± 39		348.7+0.3.....	-167.6, -165.5	3.8 ± 3.7	
	+121.2, +129.4	15 ± 10			-118.1, -114.0	15 ± 11	
12.0-0.1.....	-3.6, +10.8	77 ± 42			-42.8, -34.5	17 ± 13	
	+29.4, +41.7	62 ± 32		349.7+0.2.....	-113.6, -97.1	64 ± 32	
	+64.5, +68.5	11 ± 10			-55.9, -53.8	3.7 ± 2.5	
	+91.3, +105.7	30 ± 12		351.2+0.1.....	-221.2, -219.1	0.6 ± 0.4	
	+110.9, +139.7	69 ± 32		352.7-0.1.....	-62.4, -43.8	74 ± 27	
20.0-0.2.....	+54.7, +58.8	31 ± 30		357.7-0.1.....	-104.1, -89.7	5.8 ± 4.7	
	+98.0, +100.0	9.7 ± 9.6			-58.8, -54.7	7.6 ± 5.9	
23.3-0.3.....	...	...			+15.5, +23.7	42 ± 27	5
27.4+0.0.....	+75.8, +79.9	13 ± 12		357.7+0.3.....	-177.4, -175.3	1.8 ± 1.9	
29.7-0.3.....	+61.0, +69.2	23 ± 14					
	+96.0, +100.1	16 ± 14					

NOTES.—(1) No mapping has been carried out. (2) Excess emission in parentheses is not greater than the rms fluctuation of the surrounding pixels, but is listed because of its relatively strong peak at the position of the SNR. (3) High-resolution H I observations have been done by Giovanelli & Haynes 1979 and Braun & Strom 1986. (4) Excess emissions are determined using the map of G348.7+0.3. (5) Excess emissions are determined using the map of G357.7-0.1.

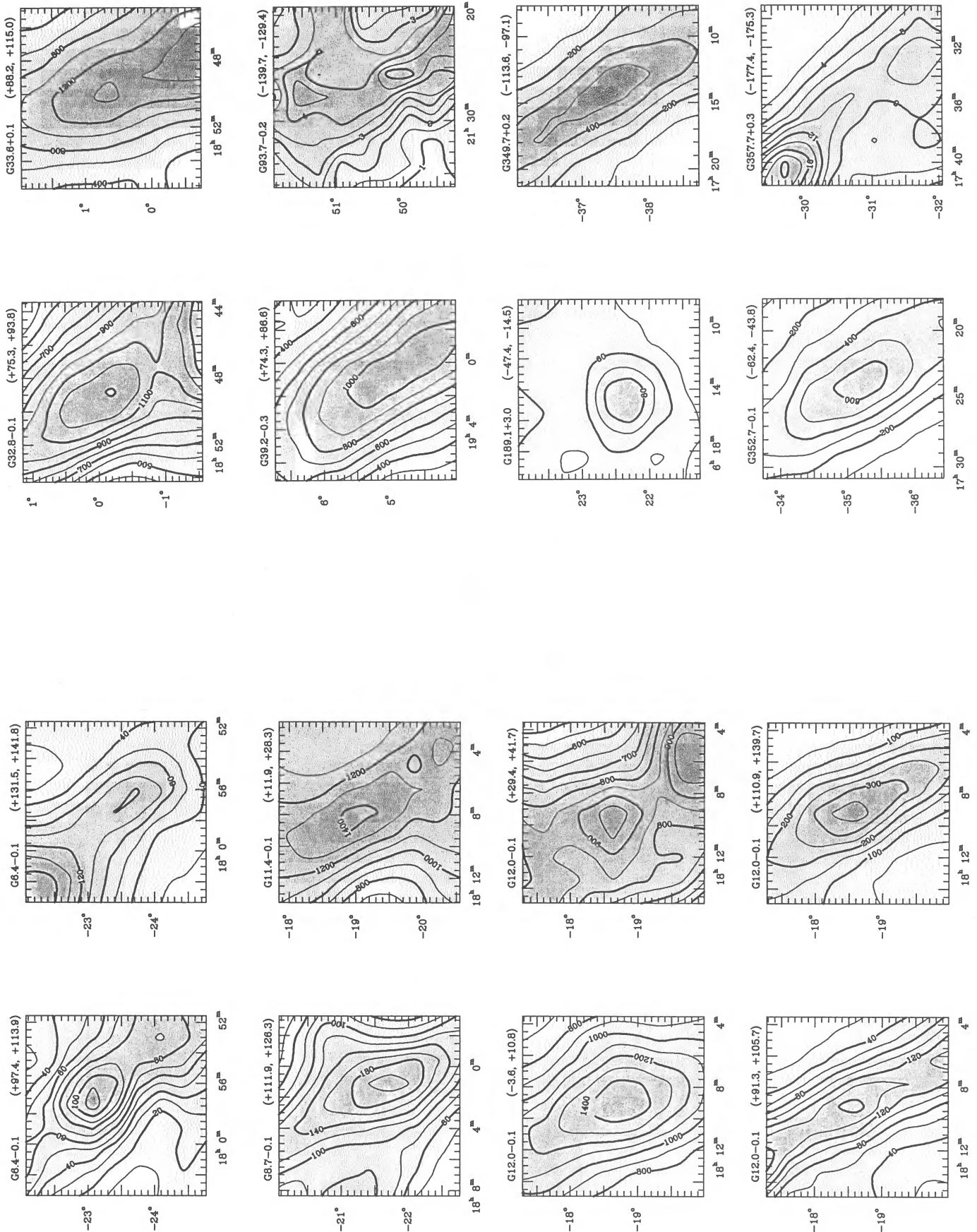


FIG. 2.—Contour maps of the integrated antenna temperature of the rank 2 SNRs with wide excess emissions ( $\geq 10 \text{ km s}^{-1}$ ). The gray-scale plot distinguishes between valley and hill, and the higher integrated intensity is blacker. The source name and the velocity range appear at the top of each picture.

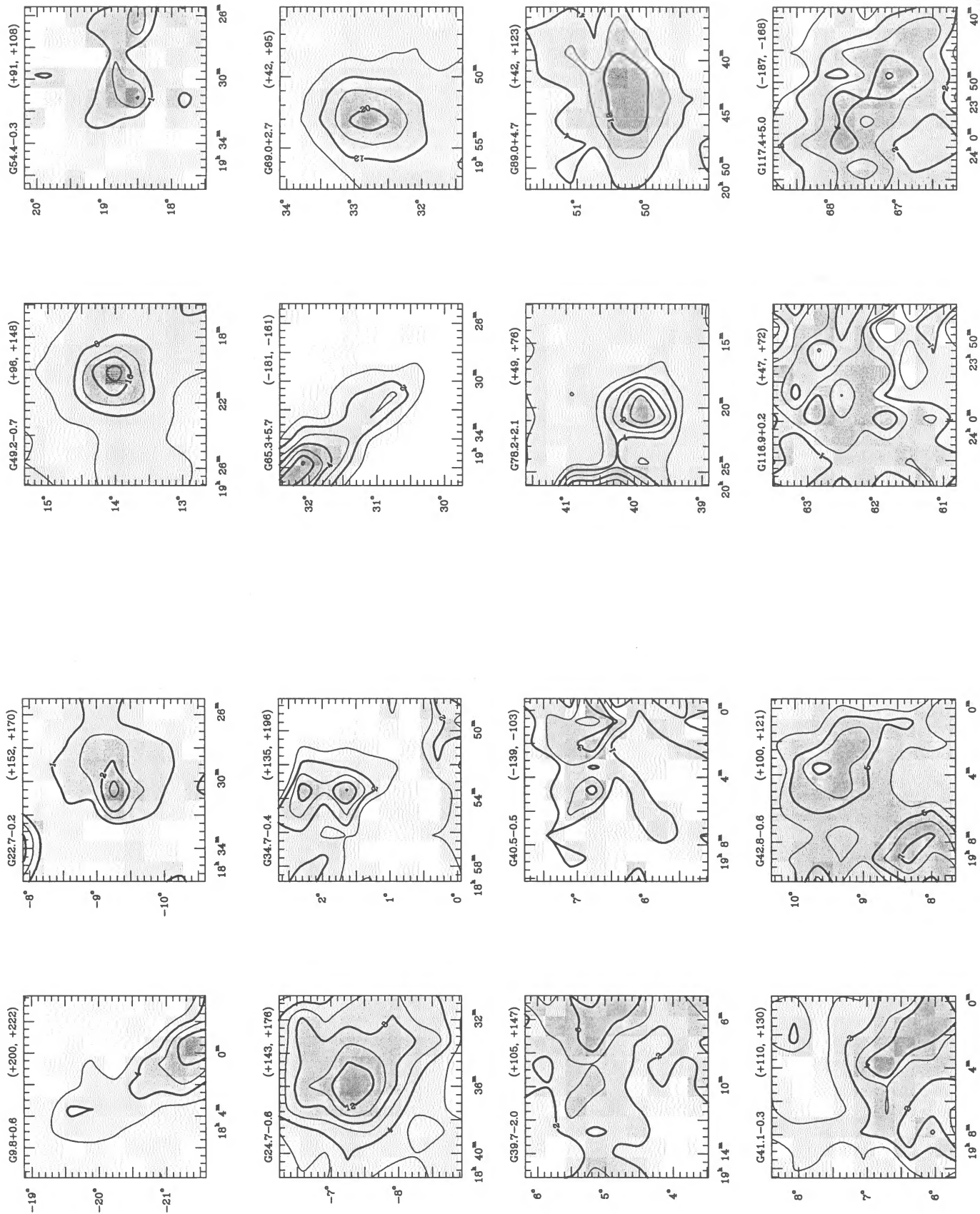


FIG. 3.—Same as Fig. 2, but for all rank 3 SNRs

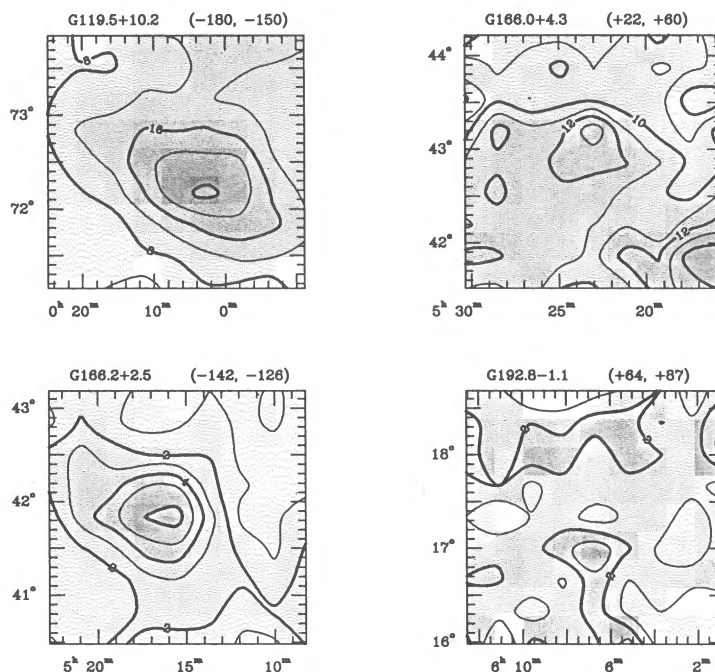


FIG. 3—Continued

cross-pattern survey. In Table 3 the average excess integrated antenna temperature in the region 1.5 times larger than the remnant is also given. Figure 3 shows maps of integrated antenna temperature for each source. The lower velocity limit of some of the maps in Figure 3 has been selected to show the high-velocity emission clearly.

In two rank 3 sources, G9.8+0.6 and G41.1-0.3 (3C 397), the high-velocity emission is continuously distributed along the Galactic plane, and therefore is probably the background emission (see also § 3.2). In G40.5-0.5, the excess emission at negative velocity occurs over a large area at the northwest of the SNR, and is probably also a background emission. In G42.8+0.6, the high-velocity emission is isolated, but peaks well outside the SNR and therefore is probably not associated with the SNR. [The peak occurs at (19<sup>h</sup>04<sup>m</sup>, +9°36'), and there is no corresponding known SNR.] In G65.3+5.7, the excess emission is due to a nearby high-velocity cloud (HVC 66+5-179 in the catalog of Hulsbosch & Wakker 1988).

The other 15 rank 3 sources appear to have associated high-velocity H I gas (see also Table 4). Two sources, G69.0+2.7 (CTB 80) and G89.0+4.7 (HB 21), are large enough to show a velocity structure implying an expanding shell. One source, G49.2-0.7 (W51), shows an exceptionally strong excess emission, and its channel maps suggest an expanding shell. One source, G24.7-0.6, shows a velocity structure implying an expanding shell, but the emitting region is much larger than the SNR, and the high-velocity emission is probably associated with a nearby H II region complex. For four sources, G22.7-0.2, G34.7-0.4 (W44), G54.4-0.3 (HC 40), and G166.0+4.3 (VRO 42.05.01), we do not have enough resolution to observe their structure. Four sources, G78.2+2.1, G117.4+5.0, G119.5+10.2 (CTA 1), and G166.2+2.5 (OA 184) show high-velocity gas inside the SNR, but they do not show the velocity structure for an expanding shell, which suggests that the high-velocity H I gas is probably either a fragment of a SNR shell or a preexisting clump accelerated by the

TABLE 3  
HIGH-VELOCITY EXCESS EMISSIONS AT RANK 3 SUPERNOVA REMNANTS

Galactic Coordinates	$v_{\min}, v_{\max}$ (km s <sup>-1</sup> )	$\int \Delta \bar{T}_A dv$ (K km s <sup>-1</sup> )	Notes	Galactic Coordinates	$v_{\min}, v_{\max}$ (km s <sup>-1</sup> )	$\int \Delta \bar{T}_A dv$ (K km s <sup>-1</sup> )	Notes
9.8+0.6.....	+200, +222	0.3 ± 1.5	1	65.3+5.7.....	-181, -161	0.0 ± 2.5	6
22.7-0.2.....	+140, +170	1.4 ± 2.3	2	69.0+2.7.....	+42, +95	3.9 ± 4.7	2
24.7-0.6.....	+143, +176	2.2 ± 2.5	3	78.2+2.1.....	+49, +76	1.3 ± 2.1	2
34.7-0.4.....	+117, +196	2.5 ± 4.0	2	89.0+4.7.....	+42, +123	3.3 ± 4.5	2
39.7-2.0.....	+112, +147	0.3 ± 1.4	4	116.9+0.2.....	+47, +72	0.4 ± 0.8	4
40.5-0.5.....	-139, -103	0.0 ± 1.1	1	117.4+5.0.....	-187, -168	1.1 ± 1.4	2
41.1-0.3.....	+110, +130	0.0 ± 1.1	1	119.5+10.2.....	-180, -150	4.7 ± 5.8	2
42.8+0.6.....	+109, +121	0.2 ± 0.8	5	166.0+4.3.....	+22, +60	1.5 ± 1.2	2
49.2-0.7.....	+73, +148	24 ± 27	3	166.2+2.5.....	-142, -126	1.2 ± 1.7	2
54.4-0.3.....	+86, +108	0.9 ± 0.9	2	192.8-1.1.....	+64, +87	0.4 ± 1.1	4

NOTES.—(1) Probably background emission. (2) Probably SNR shell. See text and Table 4. (3) High-velocity gas probably associated with nearby H II region. See text and Table 4. (4) High-velocity gas possibly associated with SNR. Not enough sensitivity. (5) High-velocity gas probably not associated with SNR. (6) High-velocity gas associated with nearby high-velocity cloud.

SN blast wave. Note that these four SNRs are large enough ( $\geq 60'$ ) to show the velocity structure if there were an expanding shell. For three sources, G39.7–2.0 (W50), G116.9+0.2 (CTB 1), and G192.8–1.1, H I maps suggest high-velocity gas at the SNR, but the sensitivity is not enough. We need more sensitive observations for these three sources.

### 3.2. Some Statistical Properties

Figure 4 shows the number of SNRs in each rank for different types of SNRs. All rank 3 SNRs having known types are “shell” SNRs; 24% of all “shell” SNRs that we surveyed have rank 3. This result is not particularly surprising, because 86% of SNRs having known types are “shell” SNRs. The a priori probability that no “F” or “C” type of SNR was assigned rank 3 is about 3%.

Figure 5 shows the radio continuum flux (at 1 GHz) of SNRs as a function of their angular diameters. In Figure 5 rank 0 and rank 1 sources are both marked by crosses, whereas rank 2 and rank 3 sources are marked by open and filled circles, respectively. In Figure 5 we have also plotted the lines of constant brightness temperature  $T_b = 10, 100, \text{ and } 1000 \text{ K}$  at 1.4 GHz. The brightness temperature at 1.4 GHz is estimated from

$$T_b = \frac{\lambda^2 S_{\nu=1.4 \text{ GHz}}}{2k \Delta\Omega} \approx 200 \left( \frac{S_{\nu=1 \text{ GHz}}}{\text{Jy}} \right) \left( \frac{\Theta}{\text{arcmin}} \right)^{-2} \text{ K}, \quad (1)$$

where  $S_\nu$  is the flux at frequency  $\nu$ ,  $k$  is the Boltzmann constant,  $\Delta\Omega$  is the solid angle occupied by the source, and  $\Theta$  is the angular diameter of the source. In the last step, we assumed  $S_\nu \propto \nu^{-0.5}$  and  $\Delta\Omega \approx \pi(\Theta/2)^2$ . We used the angular size in Table 1 as the diameter if the SNR is circular or the geometrical mean of the angular sizes if the SNR is elongated.

According to Figure 5, most (80%) rank 3 SNRs have a brightness temperature less than 10 K. This seems to be consistent with an idea that the SNRs with lower surface brightness are older (see § 4.2), because the rank 3 SNRs are believed to be old SNRs. However, this is not statistically significant because 62% of all 103 SNRs are fainter than  $T_b = 10 \text{ K}$ . In contrast to rank 3 SNRs, most (68%) rank 2 SNRs have a brightness temperature greater than 10 K. This is because rank 2 SNRs are crowded in the inner Galaxy (see § 3.3) and the SNRs in the

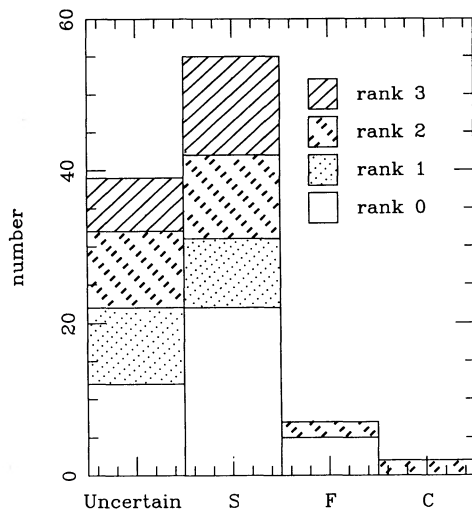


FIG. 4.—Number of SNRs in each rank for different types of SNRs. “S,” “F,” and “C” represent SNRs with “shell,” “filled-center,” and “composite” radio structure, respectively.

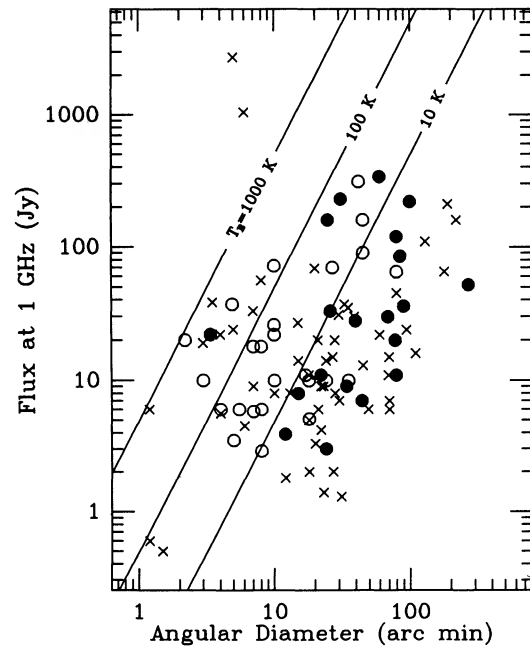


FIG. 5.—Radio continuum flux (at 1 GHz) of SNRs vs. their angular diameters. Rank 0 and rank 1 sources are both marked by crosses, whereas rank 2 and rank 3 sources are marked by open and filled circles, respectively. The solid lines represent constant brightness temperature  $T_b = 10, 100, \text{ and } 1000 \text{ K}$  at 1.4 GHz.

inner Galaxy are brighter. (The median value of  $T_b$  of 62 SNRs between  $l = 300^\circ$  and  $l = 60^\circ$  is 12 K, which is considerably larger than the median value 1.4 K of 40 SNRs between  $l = 60^\circ$  and  $l = 300^\circ$ .)

### 3.3. Distribution in $(l, v)$ -Plane

Figure 6 shows the distribution of rank 2 (open circle) and rank 3 (filled circle) sources in the  $(l, v)$ -plane, where the area of the circle is proportional to the intensity of excess emission. (Most rank 3 sources have a much smaller excess emission compared with the rank 2 sources, and therefore they appear as simple error bars.) The velocity range of excess emissions is marked by error bars. It should be noted that the error bars represent the velocity extent observed in H I, and the true velocity extent can be larger than the error bars. For rank 2 SNRs it can be larger in both directions, whereas for rank 3 SNRs it can be larger only in one direction, toward  $v_{\text{LSR}} = 0 \text{ km s}^{-1}$ . (If rank 3 SNRs have a complete expanding shell, the total velocity extent will be either  $2|v_{\text{max}} - v_0|$  or  $2|v_{\text{min}} - v_0|$ , where  $v_0$  is the systematic velocity of SNRs, depending on whether the excess emission occurs at positive or negative velocity.) In Figure 6 we have also plotted the boundary (solid lines) where the velocity is permitted by the Galactic rotation, together with lines of constant Galactic radius (dotted lines). The outer boundary is defined by the Galactic radius  $R_G = 30 \text{ kpc}$ . We assume a flat rotation curve with  $R_\odot = 8.5 \text{ kpc}$  and  $V_\odot = 220 \text{ km s}^{-1}$  in this paper. The Galactic rotation curve varies very slowly between 2 kpc and 15 kpc from the Galactic center, and the flat rotation curve seems to be a reasonable approximation for  $l \gtrsim 15^\circ$  (see Fich, Blitz, & Stark 1989).

Figure 6 shows that the velocity extents of excess emissions in all rank 3 SNRs are not permitted by the Galactic rotation model. However, care has to be taken, because the maximum velocity of excess emission has been measured at  $T_A \approx 0.06 \text{ K}$ ,

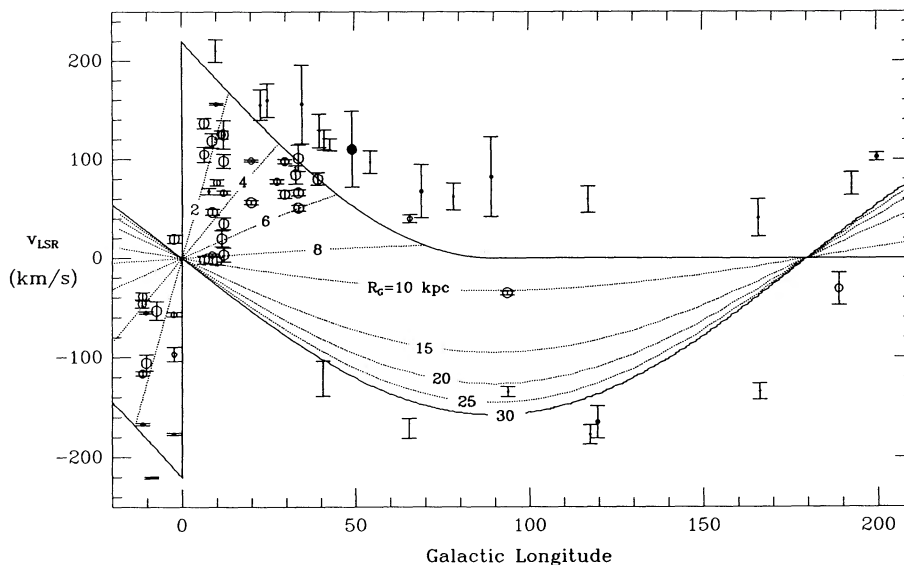


FIG. 6.—Distribution of rank 2 (open circle) and rank 3 (filled circle) sources in the  $(l, v)$ -plane. The area of the circle is proportional to the intensity of excess emission (saturated at  $\int \Delta T_A dv = 25 \text{ K km s}^{-1}$ ). The velocity range of excess emission is marked by error bars. The area bounded by two solid curves is where the velocity is permitted by the Galactic rotation. The outer boundary is defined by the Galactic radius  $R_G = 30 \text{ kpc}$ . The dotted lines represent constant Galactic radius.

and H I lines, in general, have a tail at this level (e.g., Kulkarni & Fich 1985). In G9.8+0.6 and G41.1-0.3, for example, the high-velocity emission is distributed continuously along the Galactic plane, and is likely due to a tail of the background emission. Hence, in addition to the high velocity, it is important to identify an isolated structure in order to associate H I emission with a SNR.

About 10% of the observed SNRs between  $l = 340^\circ$  and  $60^\circ$  are ranked 3, whereas 23% of the observed SNRs between  $l = 60^\circ$  and  $l = 270^\circ$  are ranked 3. The relatively small fraction of rank 3 SNRs at small Galactic longitude may reflect that the detection of an expanding SNR shell is limited by the background confusion.

Another noticeable feature in Figure 6 is the crowding of rank 2 sources between  $l = 340^\circ$  and  $l = 40^\circ$ : 83% of rank 2 SNRs are in this region. The boundary is rather well defined by  $R_G = 6 \text{ kpc}$ . This partly reflects the general crowding of SNRs inside the solar circle. However, if we consider all the observed

SNRs, the fraction is 50%, which is considerably smaller. The relatively large fraction of rank 2 SNRs in this region is most likely due to the confusion, i.e., the long path length gives a high probability for the random fluctuations of the background emissions to produce rank 2 sources.

#### 4. SUPERNOVA REMNANTS WITH ASSOCIATED HIGH-VELOCITY H I GAS

##### 4.1. Derivation of Physical Parameters

Table 4 lists various parameters for the 15 sources. The rest velocity,  $v_0$ , of G24.7-0.6 is assumed to be  $+110 \text{ km s}^{-1}$ , which is an average velocity of a nearby H II region complex (Downes et al. 1980; see § 4.4.2). The rest velocities of four SNRs, G34.7-0.4, G49.2-0.7, G116.9+0.2, and G166.2+2.5, are previously known from either H I absorption features or H $\alpha$  filaments (Sato 1973, 1974; Lozinskaya 1981). With their

TABLE 4  
PARAMETERS FOR HIGH-VELOCITY H I GAS ASSOCIATED WITH SUPERNOVA REMNANTS

Galactic Coordinates	$v_0$ (km s $^{-1}$ )	$d$ (kpc)	$v_{\text{exp}}$ (km s $^{-1}$ )	$R$ (pc)	$t_d$ ( $10^4$ yr)	$\Delta M_{\text{H I}}$ ( $M_\odot$ )	$\Delta E_K$ ( $10^{49}$ ergs)	$M_{\text{H I}}$ ( $M_\odot$ )	$n_0$ (cm $^{-3}$ )	$E_K$ ( $10^{50}$ ergs)	$E_0$ ( $10^{51}$ ergs)	References
G22.7-0.2	+56	3.9	114	15	3.9	$40 \pm 20$	$0.5 \pm 0.3$	...	...	...	...	1
G24.7-0.6	+110	9.3	66?	120	53	$4.6 \pm 0.7 \times 10^4$	$200 \pm 30$	$2.4 \times 10^5$	1.4	100	110	2
G34.7-0.4	+43	2.9	153?	14	2.7	$70 \pm 30$	$1.5 \pm 0.6$	...	...	...	...	3
G39.7-2.0	+71	5.0	76?	70	27	$170 \pm 90$	$1.0 \pm 0.5$	...	...	...	...	4
G49.2-0.7	+53	5.1	95	19	5.9	$1.1 \pm 0.4 \times 10^3$	$10 \pm 4$	$5.3 \times 10^3$	7.5	4.8	3.6	5
G54.4-0.3	+35	3.3	73	19	7.6	$45 \pm 9$	$0.24 \pm 0.05$	...	...	...	...	1
G69.0+2.7	+13	2.0	82	19	6.8	$230 \pm 20$	$1.5 \pm 0.1$	$1.3 \times 10^3$	1.8	0.87	0.56	6
G78.2+2.1	+5	1.4	71?	12	5.0	$25 \pm 4$	$0.13 \pm 0.02$	...	...	...	...	1
G89.0+4.7	-1	1.1	124	19	4.5	$150 \pm 10$	$2.3 \pm 0.2$	$1.9 \times 10^3$	2.7	2.9	1.6	1
G116.9+0.2	-35	3.2	107?	16	4.4	$12 \pm 8$	$0.14 \pm 0.09$	...	...	...	...	7
G117.4+5.0	-25	2.3	162?	26	4.7	$96 \pm 14$	$2.5 \pm 0.4$	...	...	...	...	1
G119.5+10.2	-24	2.1	156?	27	5.1	$460 \pm 50$	$11 \pm 1$	...	...	...	...	1
G166.0+4.3	-17	4.2	77?	31	12	$180 \pm 30$	$1.1 \pm 0.2$	...	...	...	...	1
G166.2+2.5	-22	6.2	120?	81	20	$1.0 \pm 0.1 \times 10^3$	$14 \pm 1$	...	...	...	...	7
G192.8-1.1	+11	2.6	76?	29	11	$41 \pm 14$	$0.24 \pm 0.08$	...	...	...	...	1

REFERENCES.—(1) Milne 1979. (2) Downes et al. 1980; see text. (3) Sato 1974. (4) Romney et al. 1987. (5) Sato 1973. (6) Koo et al. 1990. (7) Lozinskaya 1981.

known rest velocities, we computed kinematic distances  $d$  assuming the flat rotation curve. The distance to G39.7–2.0 based on the kinematic model of SS 433 is 5 kpc (Romney et al. 1987). The distance of G69.0+2.7 has been estimated in various ways, and we adopt 2 kpc (see Koo et al. 1990). With their known distances, the rest velocities are computed assuming the flat rotation curve. For the other SNRs, however, a reliable estimate of their distances is not available, and we have used the empirical radio surface brightness–linear diameter ( $\Sigma$ - $D$ ) relationship of Milne (1979; his eq. [1]), although it has a large dispersion. The rest velocities of those sources are therefore correspondingly uncertain.

The expansion velocity  $v_{\text{exp}}$  is the absolute value of the difference between the maximum (or minimum if the velocity is negative) velocity in Table 3 and the systematic velocity  $v_0$ . For those sources, which either do not show the velocity structure for an expansion or do not have enough sensitivity, the expansion velocities are listed with a question mark. The radius  $R$  in Table 4 is the linear radius corresponding to the angular size in Table 1 except for G24.7–0.6. For G24.7–0.6, the emission extends to a much larger area than the SNR, and the radius of  $\sim 45'$  is determined from our H I channel map centered at  $+110 \text{ km s}^{-1}$  (see § 4.4.2). In most sources, we cannot derive sizes of H I shells from our observations, not only because our beam is large but also because at the low velocities, where the shell reaches its largest apparent size, background emission dominates.

With its expansion velocity and radius, we can determine a dynamic age of a SNR by assuming that the high-velocity H I gas has been accelerated by a SN blast wave. We assume that SNRs have evolved in a uniform medium. Then, according to Cioffi et al. (1989), the dynamic age of a SNR in a pressure-driven snowplow phase is given by  $t_d \approx 0.3R/v_{\text{exp}}$ , and the computed values are listed in Table 4.

The mass of the *observed* high-velocity H I gas inside a region with radius 1.5 times larger than the source radius,  $\Delta M_{\text{H I}}$ , is computed by integrating over the velocity range listed in Table 3. (Note that this is a small fraction of the *total* mass. See § 4.3.) The background emission is estimated from surrounding pixels and has been subtracted. The kinetic energy  $\Delta E_K$  in Table 4 is  $\Delta M_{\text{H I}} v_{\text{exp}}^2/2$ , and therefore is the kinetic energy of the *observed* H I gas if all the gas is moving at  $v_{\text{exp}}$ . As will be seen in the next section, however, the assumption of a uniform expansion velocity does not seem to be valid, and  $\Delta E_K$  in Table 4 may be overestimated by a factor of 2 or so (see § 4.3).

If the high-velocity H I gas is the very rapidly moving gas of an expanding shell, then it is only the small portion moving nearly along our line of sight and represents only a small fraction of the total mass and total kinetic energy. In order to estimate the total H I mass and total kinetic energy of an expanding shell, we must inevitably extrapolate to the lower velocities. Among 15 SNRs, four SNRs have a velocity structure implying an expanding shell, G24.7–0.6, G49.2–0.7 (W51), G69.0+2.7 (CTB 80), and G89.0+4.7 (HB 21). For these sources we obtained the total mass using the channel maps. In each map, we determined mass again inside a region 1.5 times larger than the SNR; this provided an H I mass for each velocity interval. In all four sources, the mass per unit velocity interval increases as the velocity approaches  $v_0$  (see § 4.3). The observed mass distribution can be described by a Gaussian distribution, and we obtained the total mass by fitting a Gaussian. We also assumed the mass distribution to

be symmetric with respect to  $v_0$ ; this was necessary because excess emission was visible on only one side of  $v_0$ . The kinetic energy  $E_K$  in Table 4 is  $M_{\text{H I}} v_{\text{exp}}^2/2$ .

The initial explosion energy  $E_0$  is obtained by assuming that SNRs have evolved in a uniform medium (Cioffi et al. 1989):

$$E_0 \approx 4.9 \times 10^{49} \left( \frac{n_0}{1 \text{ cm}^{-3}} \right)^{1.16} \left( \frac{v_{\text{exp}}}{100 \text{ km s}^{-1}} \right)^{1.35} \times \left( \frac{R}{10 \text{ pc}} \right)^{3.16} \text{ ergs}. \quad (2)$$

The derived values are listed in Table 4.

#### 4.2. Correlations among Physical Parameters

We have checked possible correlations among physical parameters but have found no apparent correlations. For example, there is no correlation (1) between  $R$  and  $v_{\text{exp}}$  and (2) between  $\Sigma$  and  $t_d$ , in contrast to what we expect for SNRs with similar ambient densities and similar explosion energies. (Note that the second relationship is not independent of the first for the SNRs of which the distances are determined from the  $\Sigma$ - $D$  relationship.)

It is obvious that the radius of a SNR with a large expansion velocity must be smaller, e.g.,  $R \propto (E_0/n_0)^{7/25} v_{\text{exp}}^{-2/5}$  if  $R \propto t^{2/7}$ . In addition, the radio surface brightness of an older SNR is expected to be weaker if the nonthermal radio emission in old SNRs is due to the compression of the interstellar magnetic field and relativistic particles (van der Laan 1962; Chevalier 1974), e.g.,  $\Sigma \propto R(n_0 v_{\text{exp}}^2)^{(1-2\alpha)/2} \propto E_0^{3/5} n_0^{2/5} t^{-8/7}$ , where  $\alpha \sim -0.5$  is the spectral index ( $I_\nu \propto \nu^\alpha$ ).

The SN explosion energy is believed to be roughly a constant,  $\sim 10^{51}$  ergs, to within a factor of 3 or so (Reynolds 1988). Then the lack of correlation may suggest that the physical conditions in an ambient medium are different for different SNRs. For example, the ambient density is *not* likely to be the same for all SNRs, unless they have swept up a sufficiently large volume of interstellar space. For Types II and Ib, the size of the shell may be set by the H II region produced by a progenitor star, which varies substantially for  $M_* \lesssim 20 M_\odot$  (McKee, Van Buren, & Lazareff 1984). Also, if the observed high-velocity H I gas is a clump accelerated by a blast wave instead of a more or less complete SNR shell, then the velocity will depend not only on its density but also on its initial position with respect to the supernova.

Alternatively, the lack of correlation may be partly due to uncertain distances, in particular those based on the  $\Sigma$ - $D$  relationship. An independent estimate of the distances to the rank 3 SNRs can be made from their observed maximum (or minimum if negative) velocities and sizes using equation (2). Again we use the angular size in Table 1 as the diameter if the SNR is circular, or the geometrical mean of the angular sizes if the SNR is elongated, except for G24.7–0.6, for which we use  $90'$  as a diameter. We assume that the expansion velocity is equal to the absolute value of the observed maximum (or minimum if negative) velocity minus the rest velocity. Note that the expansion velocity implicitly depends on the distance through the rest velocity. We further assume that  $E_0 \approx 10^{51}$  ergs and  $n_0 \approx 1 \text{ cm}^{-3}$ . The dynamic distances derived in this way are listed in Table 5 together with their corresponding rest velocities. According to Table 5, the agreement between the dynamic distance and the distance based on other methods (Table 4) is very good (two distances differ by less than 10% from their mean) for G117.4+5.0, G166.0+4.3, and

TABLE 5  
DYNAMIC DISTANCES TO SUPERNOVA REMANTS WITH ASSOCIATED HIGH-VELOCITY GAS

Galactic Coordinates	$v_0$ (km s $^{-1}$ )	$d$ (kpc)	Galactic Coordinates	$v_0$ (km s $^{-1}$ )	$d$ (kpc)
G22.7-0.2.....	+120	9.2	G89.0+4.7.....	-3	1.5
G24.7-0.6.....	+20	1.7	G116.9+0.2.....	-51	4.8
G34.7-0.4.....	+85	5.5	G117.4+5.0.....	-23	2.1
G39.7-2.0.....	+27	1.9	G119.5+10.2.....	-18	1.6
G49.2-0.7.....	+47	7.2	G166.0+4.3.....	-18	4.5
G54.4-0.3.....	+41	5.3	G166.2+2.5.....	-10	2.0
G69.0+2.7.....	+15	3.1	G192.8-1.1.....	+11	2.6
G78.2+2.1.....	+1	3.3			

NOTE.—For the derivation distances and the corresponding systematic velocities see § 4.2.

G192.8-1.1, and is good (<30%) for G49.2-0.7, G54.4-0.3, G69.0+2.7, G89.0+4.7, G116.9+0.2, and G119.5+10.2. The fair agreement between the two, however, does not necessarily imply that the distance is accurate because the dynamic distance is based on the assumption of a SNR with  $E_0 = 10^{51}$  ergs in an idealized uniform medium with  $n_0 = 1$  cm $^{-3}$ . In our opinion, the dynamic distances given in Table 5 may be compared with other distance estimates, but should not be given too much weight.

#### 4.3. Mass Distribution

In all four sources for which we could obtain the mass distribution, the mass per unit line-of-sight velocity interval,  $M(v_\ell)$ , where  $v_\ell$  is the line-of-sight velocity with respect to  $v_0$ , increases as  $v_\ell$  approaches to zero. This is shown graphically in Figure 7, where the  $x$ -axis is  $v_\ell$  normalized by its expansion velocity, and the  $y$ -axis is the normalized mass per unit line-of-sight velocity interval, i.e., the mass between  $v_\ell - 0.035v_{\text{exp}}$  and  $v_\ell + 0.035v_{\text{exp}}$  normalized by the total mass with  $v_\ell$  greater than  $0.36v_{\text{exp}}$ . Figure 7 shows that the mass distribution with more mass at lower line-of-sight velocities is a characteristic common to all four sources, though the slope may be slightly different for each source. This mass distribution was previously noted for IC 443 by Giovanelli & Haynes (1979) and for CTB 80 by Koo et al. (1990). The fact that it is common to all sources with different sizes and with different expansion velocities strongly suggests that it is not due to a characteristic

special to each source, but is probably due to a characteristic of the general interstellar medium.

If the shell is expanding with a uniform velocity and has a uniform density,  $M(v_\ell)$  is independent of  $v_\ell$  except for the narrow velocity range due to the finite line width of H I lines. Hence, Figure 7 implies that either the velocity inside the shell is not uniform or the density inside the shell is not uniform, or both.

We first consider whether a systematic density and velocity gradient inside the shell can reproduce Figure 7. The mass distribution for an expanding shell with a velocity and density distribution resembles a trapezoid. This can be easily understood by the following consideration: If the shell is very thin and expands with a constant velocity  $v_{\text{exp}}$ , then the mass distribution  $M(v_\ell)$  is a rectangle with velocity extent from  $v_\ell = -v_{\text{exp}}$  to  $+v_{\text{exp}}$  and with height proportional to the mass of the shell  $M_s$ , i.e.,  $M(v_\ell) = M_s/(2v_{\text{exp}})$  (e.g., Bertout & Magnan 1987). A thick shell with expansion velocity varying from  $v_1$  to  $v_2 (>v_1)$  can be considered as a sum of many thin shells moving at constant velocities, so that the mass distribution will be the sum of rectangles with velocity extent varying from  $2v_1$  to  $2v_2$  and with heights proportional to the mass inside each thin shell. Hence, the mass distribution from a thick shell looks like a trapezoid, flat between  $v_\ell = -v_1$  and  $+v_1$ , and declining from  $v_\ell = |v_1|$  to  $|v_2|$ . It is straightforward to show that the slope between  $v_1$  and  $v_2$  is given by  $M(v_\ell) \propto v_\ell^{[(3+l_\rho)/l_v]-1}$ , if  $v(r) \propto r^{l_v}$  and  $\rho(r) \propto r^{l_\rho}$ . Hence, the mass distribution in Figure 7, which varies as  $M(v_\ell) \propto v_\ell^{-3}$  between  $0.4v_{\text{exp}}$  and  $v_{\text{exp}}$ , can be explained by a systematic density and velocity gradient inside the shell if  $l_v \approx -(3+l_\rho)/2$ . Note that Figure 7 also implies that the minimum velocity  $v_1$  is less than  $\sim 0.5v_{\text{exp}}$ , because there is no indication of turnoff to a flat distribution at  $v_\ell = 0.5v_{\text{exp}}$ .

If there is a systematic density and velocity gradient, another constraint on  $l_\rho$  and  $l_v$  may be obtained from the line profile at the central position. If an expanding shell is resolved, the line profile at the central position is proportional to the column density per unit velocity interval, so that  $T_A(v_\ell) \propto v_\ell^{[(1+l_\rho)/l_v]-1}$ , or  $T_A(v_\ell)/M(v_\ell) \propto v_\ell^{-2/l_v}$ . Hence, if we map a SNR at high angular resolution, in principle we can determine the power indices for the density and velocity distribution inside the shell. For CTB 80, such a high angular resolution (3'3) map is available, and the line profiles near the central position show smooth bumps at high positive velocities (Fig. 5 of Koo et al. 1990). Koo et al. showed that an expanding shell with a uniform expansion velocity and with large random motions may explain the broad central line profile, but cannot explain the observed mass distribution. Figure 8 shows the ratio (*filled*

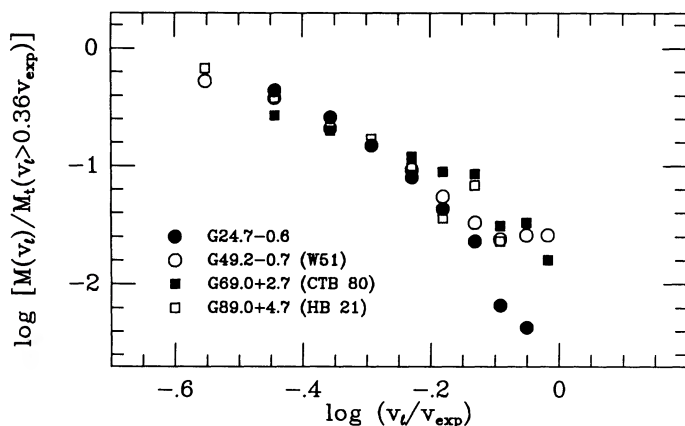


FIG. 7.—Mass per unit line-of-sight velocity interval,  $M(v_\ell)$ , where  $v_\ell$  is the line-of-sight velocity with respect to  $v_0$ , in four rank 3 SNRs. The  $x$ -axis is  $v_\ell$  normalized by its expansion velocity, and the  $y$ -axis is the normalized mass per unit line-of-sight velocity interval, i.e., mass between  $v_\ell - 0.035v_{\text{exp}}$  and  $v_\ell + 0.035v_{\text{exp}}$  normalized by the total mass with  $v_\ell$  greater than  $0.36v_{\text{exp}}$ .

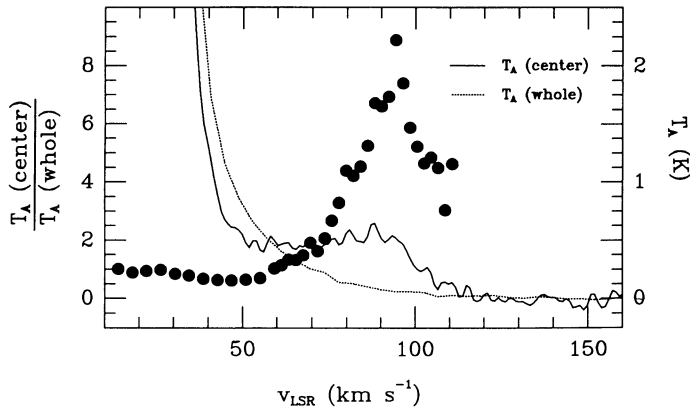


FIG. 8.—Ratio (filled circles) of the average profile near the center ( $R < 5'$ ; solid line) to the average profile of the whole SNR ( $R < 32'$ ; dotted line), in CTB 80 (Koo et al. 1990).

circles) of the average profile near the center ( $R < 5'$ ) to the average profile of the whole SNR ( $R < 32'$ ), which corresponds to the mass distribution. The ratio certainly increases with velocity between  $v_{\text{LSR}} = +50$  and  $+95 \text{ km s}^{-1}$ , where the emission is not contaminated by the background emission. The slope is very well described by  $T_A(\text{center})/T_A(\text{whole}) \propto v_r^{3.4}$ , where  $v_r$  is the velocity with respect to the rest velocity of CTB 80,  $v_0 = +13 \text{ km s}^{-1}$ . Therefore, if we assume that the random motion is much smaller than the expansion velocity, the slope implies the power index for the velocity distribution  $l_v \approx -0.6$ . Then, since  $l_v \approx -(3 + l_\rho)/2$ , the power index for the density distribution is  $l_\rho \approx -1.8$ .

Hence, an expanding shell with both the density and the velocity decreasing outward seems to be consistent with the observed properties in Figure 7. However, in order for the minimum velocity  $v_1$  to be less than  $\sim 0.5v_{\text{exp}}$ , the relatively small  $l_v$  implies a very thick shell,  $\Delta R/R \gtrsim 0.7$ , which is much larger than the thickness  $\Delta R/R \lesssim 0.3$  of the CTB 80 shell in infrared (Fesen et al. 1988).

An alternative explanation for the observed mass distribution, which we prefer, is that the shell is composed of clumps in addition to a smoothly distributed gas. In this case, a heavier cloud will experience a smaller acceleration, and therefore a mass distribution of clouds will naturally result in a large velocity dispersion. The clumpy shell structure has been observed in CTB 80 (Koo et al. 1990), and it is also consistent with the characteristics of a multiphase interstellar medium, i.e., cloud and intercloud medium.

If Figure 7 is indeed due to a mass distribution of clouds, then the slope  $M(v) \propto v_r^{-3}$  should tell us about the slope of the cloud mass distribution  $N(m) \propto m^\beta$ , the number of clouds per unit mass. If we assume that each cloud of mass  $m$  is moving at the same velocity  $v(m)$  and there is a relation  $mv(m)^\beta \sim \text{constant}$ , then the mass per unit velocity interval  $M(v)$  is proportional to  $mN(m)(dm/dv) \sim v^{-(\beta+2)\beta-1}$ . For  $\beta = 2$  (constant kinetic energy), the observed slope implies  $N(m) \propto m^{-1}$ , whereas for  $\beta = 1$  (constant momentum),  $N(m)$  is independent of the cloud mass. The assumption of the same velocity for clouds with equal mass, however, does not seem to be valid: First, the clouds at larger distances from the explosion center are less accelerated because the blast wave weakens as it expands. Second, according to McKee, Cowie, & Ostriker (1978), clouds are continuously accelerated by the passage of high-velocity shocked intercloud medium, and the current

velocity and the location of a cloud depend on the cloud's initial location. Hence, even if two clouds have the same mass, their velocities can differ depending on their initial position. The correlation between the observed  $M(v)$  and the cloud mass distribution remains to be explored.

Regardless of its cause, the mass distribution in Figure 7 implies that the kinetic energy of H I shells derived by assuming a constant expansion velocity  $v_{\text{exp}}$  is overestimated. For  $M(v) \sim v^{-3}$ , the factor is

$$\frac{\int M(v)v^2 dv}{\int M(v) dv v_{\text{exp}}^2} \sim 2 \ln \left( \frac{v_{\text{exp}}}{v_1} \right) \left/ \left[ \left( \frac{v_{\text{exp}}}{v_1} \right)^2 - 1 \right] \right.,$$

which is equal to 0.46 for  $v_1 = 0.5v_{\text{exp}}$ . Hence, the kinetic energy in Table 4 is probably overestimated by a factor of  $\sim 2$ .

#### 4.4. Discussion of Individual Supernova Remnants

In the following we briefly discuss the results on each SNR in Table 4.

##### 4.4.1. G22.7-0.2

In the 2.7 GHz survey of Reich et al. (1984), G22.7-0.2 appears as a shell-like object with a size of  $26'$ . No optical filaments are seen on the Palomar red plate, and no obvious infrared emission associated with the SNR has been detected (van den Bergh 1978; Arendt 1989).

Figure 3 shows that there is a very weak unresolved excess emission centered on G22.7-0.2 between  $v_{\text{LSR}} = +150$  and  $+170 \text{ km s}^{-1}$ . (All velocities in this section are velocities with respect to the local standard of rest unless otherwise stated.) The channel maps are not very informative, and are not shown. The positional agreement within a pixel strongly suggests that the high-velocity H I gas is associated with the SNR G22.7-0.2. The source is very weak and unresolved, so that we cannot determine whether the excess emission is due to an expanding H I shell or not.

At velocities between  $+125$  and  $+190 \text{ km s}^{-1}$ , there is an enhanced H I emission at  $\alpha_{1950} \approx 18^{\text{h}}20^{\text{m}}-28^{\text{m}}$ , and  $\delta_{1950} \approx -9^\circ$  to  $-8^\circ$ , which surrounds a weak ( $T_b \approx 0.75 \text{ K}$ ) continuum source of  $40'$  size in the 21 cm map of Reich, Reich, & Fürst (1990). The association of the H I gas with this source is possible.

##### 4.4.2. G24.7-0.6

G24.7-0.6 is a small ( $\sim 15'$ ), weak nonthermal radio source located close to a complex region of  $40'$  size, which contains many H II regions (Angerhofer, Becker, & Kundu 1977). There is a radio spur which stems out from the H II region complex and is directed towards the nonthermal source G24.7-0.6 in the 2.7 GHz survey of Reich et al. (1984). The distance between the radio spur and the center of G24.7-0.6 is  $\sim 10'$  (26 pc at 9 kpc). The radio spur may suggest that G24.7-0.6 is associated with the H II region complex. The velocity of the H II region complex has been measured by Downes et al. (1980) using the H110 $\alpha$  line, and it ranges from  $+96$  to  $+118 \text{ km s}^{-1}$ . No optical filaments are seen on the Palomar red plate, and no infrared emission associated with the SNR has been detected (van den Bergh 1978; Arendt 1989).

We show that channel maps in Figure 9a. At  $v_{\text{LSR}} = +146$  to  $+167 \text{ km s}^{-1}$ , the H I emission is confined to a small region near the center. The peak, however, occurs 1 pixel ( $18'$ ) away from G24.7-0.6, which is very small ( $\sim 15'$  in diameter) in radio continuum. This suggests that the high-velocity gas is probably *not* a clump accelerated by the SN blast wave in

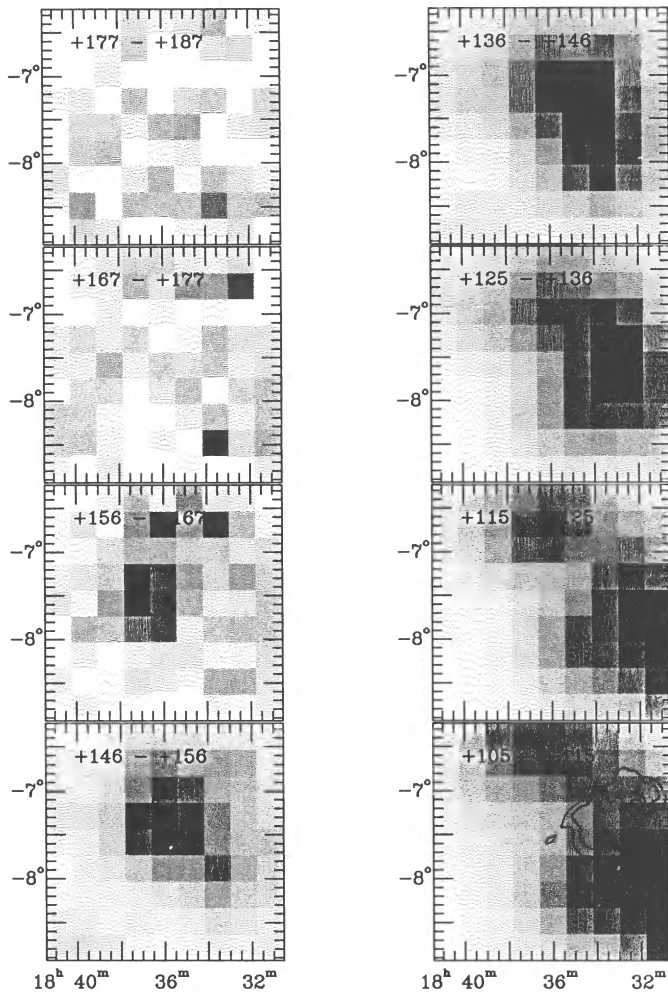


FIG. 9a

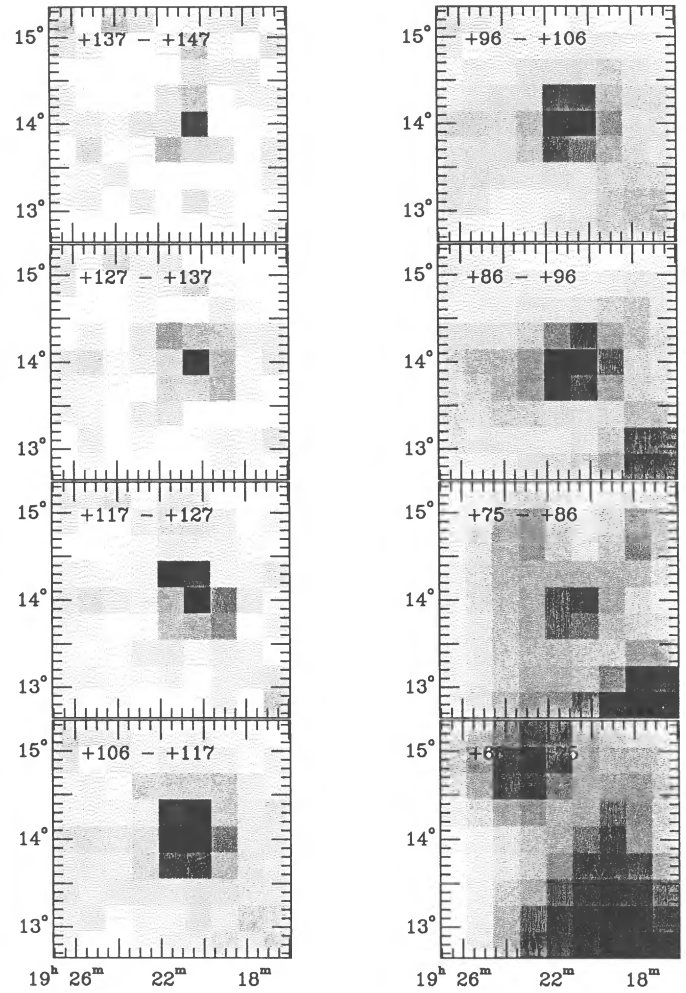


FIG. 9b

FIG. 9.—Channel maps of H I emission in (a) G24.7–0.6, (b) G49.2–0.7, and (c) G89.0+4.7. The gray scale used the minimum and maximum column densities of each channel map as the full dynamic range. The areas with larger column densities are blacker. The velocity range appears at the top of each picture. The contour map overlaid on top of the channel map centered at  $+110 \text{ km s}^{-1}$  of G49.2–0.7 is the  $T_b = 3$  and 4 K contour at 2.7 GHz (Reich et al. 1984). There is a H II region complex bounded by the 4 K contour line.

G24.7–0.6. At lower velocities, the H I gas is distributed over a large area to the west of G24.7–0.6, and the velocity structure for  $v_{\text{LSR}} > +105 \text{ km s}^{-1}$  suggests a large incomplete expanding H I shell of  $R \sim 45'$  with its eastern portion broken. Inside the H I shell-like structure, the H II region complex is located. We draw  $T_b = 3$  and 4 K contour lines at 2.7 GHz (Reich et al. 1984) in the channel map centered at  $+110 \text{ km s}^{-1}$ , and the H II region complex is bounded by the 4 K contour line. The H I structure appears to surround the H II region complex, although it is considerably larger than the H II region complex. Note that the average velocity of the recombination lines in the H II region complex is close to  $+110 \text{ km s}^{-1}$ . The agreement in position and velocity suggests that the H I structure is quite likely to be associated with the H II region complex instead of the nonthermal source G24.7–0.6.

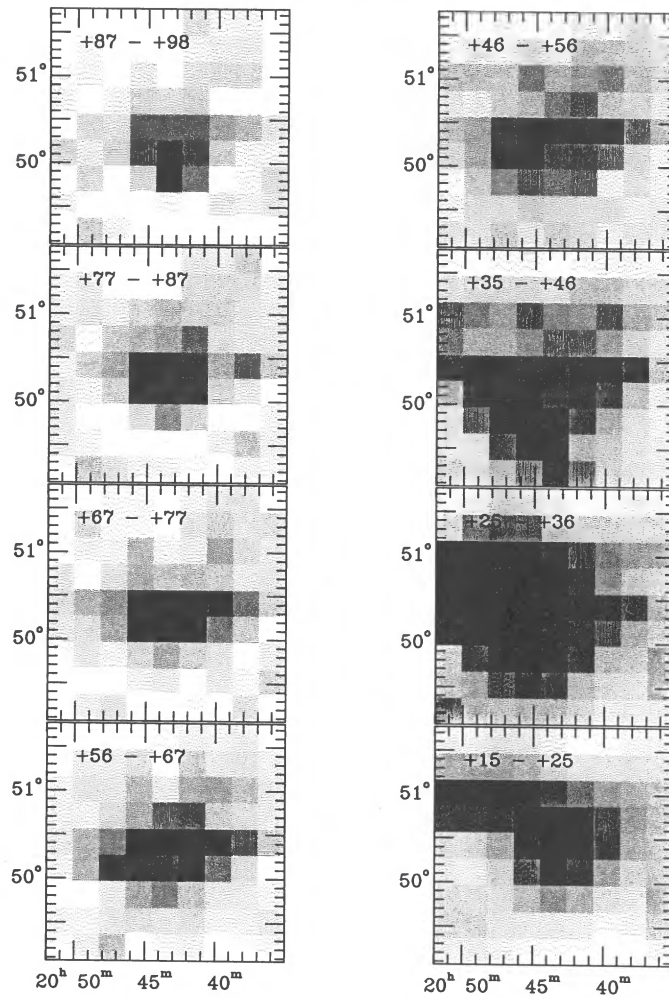
The velocity structure, however, does *not* imply a single large expanding shell around the H II region complex. It is true that the emitting region is confined to small areas at highest velocities, and becomes larger as the velocity decreases. However, from  $v_{\text{LSR}} = +167$  to  $+136 \text{ km s}^{-1}$ , the enlargement does not occur centered at the same area at highest velocities. Instead

the emitting region moves around. Hence, in conclusion, our channel maps suggest a partially complete expanding H I shell associated with the H II region complex at lower velocities, but the relation of the highest velocity gas to this shell is unclear. The high-velocity gas can be either a portion of the broken shell or a gas clump accelerated by a blast wave.

The expansion velocity  $66 \text{ km s}^{-1}$  listed in Table 4, therefore, is likely to be an overestimate for the expansion velocity of the shell, which explains the uncomfortably large kinetic energy of the shell.

#### 4.4.3. G34.7–0.4 (W44)

In the 2.7 GHz survey of Reich et al. (1984), W44 appears as an elongated shell with an enhanced region to the east. X-ray emission has been detected in the central area of the SNR by Smith et al. (1985), and implies a gas temperature of  $6 \times 10^6 \text{ K}$ . No optical filaments are seen on the Palomar red plate (van den Bergh 1978). Arendt (1989) has detected infrared emission associated with the SNR. Knapp & Kerr (1974) reported the detection of a cold H I shell expanding at  $4 \text{ km s}^{-1}$ . A molecular cloud at the east of the SNR has been observed by Wootten



(1977) and DeNoyer (1983). Wootten used line widths and velocity gradients to conclude that the CO emission originates from a dense SNR shell expanding at  $4 \text{ km s}^{-1}$ . However, the CO line profiles are composed of several components, and it is not clear whether the molecular line observations imply a dense SNR shell (DeNoyer 1983).

Figure 3 shows that there is a very weak high-velocity H I emission between  $v_{\text{LSR}} = +135$  and  $+196 \text{ km s}^{-1}$  near the SNR W44. The H I emission, however, peaks slightly north of the SNR, which implies that the high-velocity H I emission is probably not a cap portion of an expanding SNR shell but is either a portion of a broken shell or a gas clump accelerated by the blast wave.

There is a gas clump of  $10'$  size centered at  $(\alpha_{1950}, \delta_{1950} = 18^{\text{h}}53^{\text{m}}8^{\text{s}}, +1^{\circ}28')$  in Arendt's infrared map (1989), which is very close to the high-velocity H I emission peak. An average  $100 \mu\text{m}$  surface brightness is  $\sim 200 \text{ MJy sr}^{-1}$ , which implies  $4.4 \times 10^3 M_{\odot}$  for the H I mass of the gas clump using  $N_{\text{H}}/I_{100} = 10^{20} \text{ cm}^{-2}/1 \text{ MJy sr}^{-1}$ . The association of the high-velocity H I gas with this clump is very suggestive and needs to be confirmed by high-resolution H I observations.

#### 4.4.4. G39.7-2.0 (W50, SS 433)

W50 is a large ( $2^{\circ} \times 1^{\circ}$ ), elongated nonthermal shell-like source (Downes, Pauls, & Salter 1986). Near the center of the

shell structure, the extraordinary emission-line source SS 433 emitting jets in two opposing directions is located. The physical association of W50 and SS 433 is indicated by the alignment of the jets with the major axis of W50. The distance to SS 433 based on the kinematic model is 5 kpc (Romney et al. 1987). Faint optical filaments are seen at the edge of the radio emission (van den Bergh 1980). No infrared emission associated with the SNR has been detected (Arendt 1989). To the northwest of W50, an H II region, S74, is superposed, which is probably a foreground object at 2.7 kpc (Crampton, Georgelin, & Georgelin 1978).

Figure 3 shows that there is a very weak, extended high-velocity H I emission in this region. The emission is enhanced along the northwestern edge of W50, where the continuum emission is stronger. The positional coincidence of enhanced emissions is suggestive of their association.

#### 4.4.5. G49.2-0.7 (W51)

The nonthermal radio source G49.2-0.7, or W51C, is embedded in a complex region known as W51, which contains many H II regions (e.g., Bieging 1975). The H II region complex W51 has been divided into two groups, W51A and W51B, each of which consists of two major compact components. The compact components are embedded in a diffuse low surface brightness envelope. The association of the nonthermal com-

ponent W51C with the H II region complex is not clear. No optical filaments are seen on the Palomar red plate, and no infrared emission associated with the SNR has been detected (van den Bergh 1978; Arendt 1989).

We show the channel maps in Figure 9b, which clearly show the high-velocity H I gas near W51C between  $v_{\text{LSR}} = +75$  and  $+147 \text{ km s}^{-1}$ . The H I emission, however, peaks at the east of W51C, and right at the position of the less luminous H II region W51B ( $19^{\text{h}}20^{\text{m}}43^{\text{s}}.4$ ,  $13^{\circ}58'24''$ ). The most luminous H II region in the W51 complex, W51A ( $19^{\text{h}}21^{\text{m}}21^{\text{s}}.8$ ,  $14^{\circ}24'40''$ ), is slightly north of the high-velocity H I. The positional coincidence with W51B suggests that the high-velocity gas may be driven by stellar winds from W51B instead of the SN blast wave. High-resolution observations are needed.

The channel maps suggest that the size of the H I shell becomes larger as the velocity decreases, which implies that we are observing the receding portion of an expanding H I shell. The rest velocity of the W51 complex is rather well determined to be  $53 \text{ km s}^{-1}$  from H I absorption lines (Sato 1973), and the implied expansion velocity of the shell is  $95 \text{ km s}^{-1}$ .

#### 4.4.6. G54.4-0.3 (HC 40)

The 1.4 GHz map of Caswell (1985) clearly shows that G54.4-0.3 is a shell-type SNR with enhanced emission to the northwest. No filaments are seen on a H $\alpha$  plate taken with the Palomar 1.2 m Schmidt telescope, and no infrared emission associated with the SNR has been detected (van den Bergh 1978; Arendt 1989).

Figure 3 shows that there is a very weak H I emission at the position of G54.4-0.3. The H I peak occurs at the southern portion of the SNR. The positional agreement suggests that the high-velocity H I gas is possibly associated with the SNR.

#### 4.4.7. G69.0+2.7 (CTB 80)

The expanding H I shell in CTB 80 has been observed and studied in detail by Koo et al. (1990). The H I shell is clumpy and is partially complete with its southwest portion opened. The expansion velocity of the shell is  $72 \text{ km s}^{-1}$ , and its size is 19 pc assuming a distance of 2 kpc. The dynamical age of the H I shell is then  $8 \times 10^4 \text{ yr}$ , which is close to the characteristic age  $10^5 \text{ yr}$  of the pulsar PSR 1951+32 (Kulkarni et al. 1988). The shape of the H I shell matches that of the infrared shell, which has enhanced  $60 \mu\text{m}$  emission compared with its  $100 \mu\text{m}$  emission (Fesen et al. 1988). The scenario that the pulsar, which was born at the center, has caught up with the expanding SNR shell and has produced its peculiar radio morphology has been proposed by Fesen et al. (1988), Kulkarni et al. (1988), and Hester & Kulkarni (1988), and is supported by the detection of a partially complete H I shell.

#### 4.4.8. G78.2+2.1 (DR 4, $\gamma$ Cygni)

The map at 1.4 GHz by Higgs, Landecker, & Roger (1977) shows a nearly complete shell of emission centered to the northwest of  $\gamma$  Cygni. Faint optical filaments have been observed by van den Bergh (1978). H I observations on G78.2+2.1 have been previously done by Landecker et al. (1980) and Braun & Strom (1986). They found high-velocity cloudlets moving at  $v_{\text{LSR}} = +35$  to  $-68 \text{ km s}^{-1}$  in this region. There is no indication of an expanding H I shell, but the high-velocity cloudlets are likely to be accelerated by the SN blast wave. A molecular cloud which may be interacting with the SNR has been detected by Fukui & Tatematsu (1988).

Figure 3 shows the high-velocity clump mentioned above. It also shows another high-velocity clump to the east of DR 4.

We mapped this clump, and found that an unresolved excess emission occurs between  $v_{\text{LSR}} = +36$  and  $+57 \text{ km s}^{-1}$  at  $(\alpha_{1950}, \delta_{1950}) = (20^{\text{h}}27^{\text{m}}, 40^{\circ}35')$  or  $(l, b) = (79^{\circ}3, +1^{\circ}1)$ . Since the velocity is considerably larger than the maximum velocity suggested by the Galactic rotation, and the emission is isolated, the excess emission is very likely to be associated with a SNR.

#### 4.4.9. G89.0+4.7 (HB 21)

The map at 1.4 GHz by Hill (1974) shows a nearly complete shell of emission with its northern part flattened. X-ray emission from HB 21 was detected by Leahy (1987), and implies a gas kinetic temperature of  $6 \times 10^6 \text{ K}$ . Optical nebulosity is present in this region, but the correlation with radio structure is poor (Willis 1973; cf. van den Bergh 1978). Arendt (1989) has not detected obvious infrared emission associated with the SNR. Assousa & Erkes (1973) reported the detection of an H I shell expanding at  $25 \text{ km s}^{-1}$ . A giant molecular cloud east of the remnants was observed by Huang & Thaddeus (1986), Fukui & Tatematsu (1988), and Tatematsu et al. (1990). The last authors also obtained a high-resolution ( $1'$ ) H I map, which shows a H I cloud just outside the eastern boundary of HB 21 between  $v_{\text{LSR}} = -10$  and  $+17 \text{ km s}^{-1}$ . There has been no detection of high-velocity molecular gas in this region, but the interaction of the SNR with the molecular cloud and also with the H I cloud is likely.

We show the channel maps in Figure 9c. The size of the H I emitting region becomes larger as the velocity decreases until  $\sim +25 \text{ km s}^{-1}$ . At smaller velocities the H I column density suddenly increases, which implies that the background emission starts to dominate. If we determine the rest velocity of HB 21 based on Figure 9c, it will be  $\sim +30 \text{ km s}^{-1}$  where the size is the largest. This velocity, however, is much larger than the maximum velocity  $0 \text{ km s}^{-1}$  permitted by the Galactic rotation. Possibly the shell at lower velocities is obscured by the background emission. We adopt  $+3 \text{ km s}^{-1}$ , the kinematic distance based on the  $\Sigma$ - $D$  relationship, as the rest velocity of HB 21 in this paper. The velocity structure at  $v_{\text{LSR}} \gtrsim 25 \text{ km s}^{-1}$  implies that we are looking at the receding portion of a H I shell expanding at  $125 \text{ km s}^{-1}$ . This expansion velocity is much larger than that derived by Assousa & Erkes (1973). The reason is that they did not have enough sensitivity to detect the high-velocity gas, and estimated the expansion velocity from only the distribution of gas with  $v_{\text{LSR}} \lesssim 25 \text{ km s}^{-1}$ .

The H I gas in the central area of the channel map between  $v_{\text{LSR}} = +15$  and  $+25 \text{ km s}^{-1}$  looks like an isolated cloud instead of an expanding shell, because the distribution does not correlate well with H I gas at higher velocities. This cloud fits well with a hole in the central area of the channel maps between  $v_{\text{LSR}} = -6$  and  $+15 \text{ km s}^{-1}$ . If the cloud is associated with HB 21, which is very likely, based on its position and the large velocity, then the cloud might have been accelerated by the SN blast wave. Why, then, is the cloud moving much more slowly than the rest of the shell? The cloud is relatively dense. The velocity of the cloud,  $20 \text{ km s}^{-1}$ , would be commensurate with the velocity of the shell,  $125 \text{ km s}^{-1}$ , if the density of the cloud were greater than the density of the ambient medium by a factor of  $\sim (125/20)^2 \sim 40$ .

The size of the H I shell is comparable to the size of the radio shell, except that the H I shell seems to extend more to the east than does the radio shell. The apparent larger size of the H I shell is difficult to understand if the radio continuum emission originates in the postshock cooling layer where the interstellar

magnetic field and relativistic particles are compressed. In order to compare the H I and the radio continuum structure in detail, we need a sensitive higher resolution H I map.

#### 4.4.10. *G116.9+0.2(CTB 1)*

The 1.4 GHz map of Dickel & Willis (1980) shows a well-defined shell SNR with its northwestern portion opened. Optical filaments coincident with the position of the radio shell have been observed (D'Odorico & Sabbadin 1977; van den Bergh 1978; Lozinskaya 1981; Bohigas et al. 1983). Bohigas et al. estimated a shock velocity of  $90 \text{ km s}^{-1}$  from optical line ratios. Arendt (1989) has not detected any infrared emission associated with the SNR.

Figure 3 shows that there is a very weak high-velocity H I emission in this region. We do not have enough sensitivity to see the structure, but the derived expansion velocity  $107 \text{ km s}^{-1}$  is close to the shock velocity derived from optical studies, and the high-velocity H I gas is possibly associated with the SNR.

#### 4.4.11. *G117.4+5.0*

G117.4+5.0 is an extended  $\sim 1^\circ$  radio source, which includes an H II region, NGC 7822. The spectral study by Bonsignori-Facondi & Tomasi (1979) suggests the nonthermal original for the extended component. There are also faint optical nebulosities, which coincide with the extended radio emission. Lozinskaya & Sitnik (1977) found that the H $\alpha$  lines from faint optical nebulosities are split into two components: one at  $\sim -10 \text{ km s}^{-1}$ , which corresponds to the systematic velocity of NGC 7822, and another at  $\sim +30 \text{ km s}^{-1}$ . They interpreted this split as an indication of a shell expanding at  $40 \text{ km s}^{-1}$  with respect to NGC 7822. There are some enhanced infrared emissions in this region (Arendt 1989).

Figure 3 shows that there is a very weak H I emission in this region at high negative velocities. The derived expansion velocity  $162 \text{ km s}^{-1}$  is much larger than the velocity of faint optical nebulosities. The association of the high-velocity H I gas with the radio source is not clear.

There is also an enhanced H I emission ( $\Delta T_A \approx 1 \text{ K}$ ) at  $\alpha_{1950} = 23^{\text{h}}45^{\text{m}}-23^{\text{h}}50^{\text{m}}$  and  $\delta_{1950} = 66^\circ45'-67^\circ20'$  between  $v_{\text{LSR}} = +15$  and  $+26 \text{ km s}^{-1}$ . The similar velocities suggest that this gas is possibly associated with faint optical nebulosities.

#### 4.4.12. *G119.5+10.2(CTA 1)*

The 2.7 GHz map of Sieber, Haslam, & Salter (1979) shows a well-defined shell SNR of size  $R \sim 45'$  with its northwestern portion opened. Faint optical filaments coincident with the position of the radio shell have been observed by Fesen et al. (1981), who suggested a shock velocity larger than  $60 \text{ km s}^{-1}$  on the basis of strong [O III] emission. Arendt (1989) has not detected any infrared emission associated with the SNR.

Figure 3 shows that there is an isolated H I emission at high negative velocities in this region. The H I emission peak is just inside the southern portion of the radio shell. The channel maps do not show the velocity structure of an expanding shell, and the high-velocity gas is most likely to be a clump instead of an expanding shell, which is also consistent with its location relative to the radio shell.

#### 4.4.13. *G166.0+4.3(VRO 42.05.01)*

The SNR VRO 42.05.01 has a very peculiar radio structure (Landecker et al. 1982; Pineault et al. 1987). Its morphology can be divided into two components: the larger southwestern

component, which has a roughly circular segment of a shell of  $80'$  diameter, and the small northeastern component, which is an almost perfectly circular shell with a diameter of  $31'$ . The unusual radio structure led Pineault et al. (1987) to propose that the SNR is breaking out from a warm medium into a hot, tenuous interstellar cavity. Optical studies suggest a shock velocity of  $\sim 50 \text{ km s}^{-1}$  or less (Lozinskaya 1979; Pineault et al. 1985). H I observations have been done by Braun & Strom (1986), and do not show an expanding shell. Their observations, however, do show H I filaments both at high negative,  $v_{\text{LSR}} \lesssim -70 \text{ km s}^{-1}$ , and at high positive,  $v_{\text{LSR}} \gtrsim +20 \text{ km s}^{-1}$ , velocities, some of which have clear counterparts in the radio continuum. The infrared emission associated with the larger southern component of the SNR has been detected by Arendt (1989).

Figure 3 shows the presence of a weak high-velocity H I emission in this region. The position of the enhanced H I emission agrees with the SNR, and their association is quite likely. The derived expansion velocity,  $77 \text{ km s}^{-1}$ , is close to that derived from optical studies.

Since the SNR is located in the anticenter direction, there is not much confusion by the background emission, and we expect to observe high-velocity H I gas at both positive and negative velocities. Coincidentally, there are high-velocity H I emission at negative velocities,  $v_{\text{LSR}} = -100$  to  $-60 \text{ km s}^{-1}$ , in this region. However, the emission is extended over the whole field ( $2.7 \times 2.7$ ), and there is no obvious correlation with the SNR; therefore the association is not likely.

#### 4.4.14. *G166.2+2.5(OA 184)*

The 1.4 GHz map of Routledge, Landecker, & Vaneldik (1986) shows an elongated ( $1.5^\circ \times 1^\circ$ ) shell with an enhanced emission at its northwest. Arc-shaped optical filaments are seen in this region (D'Odorico & Sabbadin 1977). Lozinskaya & Sitnik (1979) obtained a mean expansion velocity of  $50 \text{ km s}^{-1}$  from their optical studies, although the gas was seen moving as fast as  $120 \text{ km s}^{-1}$ . H I observations on G166.2+2.5 have been previously done by Routledge, Landecker, and Vaneldik. Their observations covered the range  $v_{\text{LSR}} = -124$  to  $+85 \text{ km s}^{-1}$ , and showed that the H I gas at  $-30 \text{ km s}^{-1}$  coincides with the enhanced radio-emitting region and therefore is very likely to be associated with the SNR. An almost complete circular shell is clearly visible in the 60 and  $100 \mu\text{m}$  maps of Arendt (1989).

Figure 3 shows the presence of H I gas at high negative velocities,  $v_{\text{LSR}} = -142$  to  $-126 \text{ km s}^{-1}$ , in the central region of the SNR. The high velocity and the positional coincidence are very suggestive of the physical association. However, there are H I emissions at high negative velocities over the whole field, and additional evidences such as the correlation of the H I gas and the radio shell are needed to prove the physical association.

Again, since the SNR is located in the anticenter direction, we expect to observe H I gas at high positive velocities. There is no high-velocity H I emission at  $v_{\text{LSR}} > +60 \text{ km s}^{-1}$ . But there is H I gas moving at  $+30 \text{ km s}^{-1}$  and located at the position of the SNR. The velocity of the gas is close to the mean expansion velocity obtained from optical studies, and therefore the association with the SNR is possible.

#### 4.4.15. *G192.8-1.1(PKS 0607+17)*

The 1.4 GHz map of Caswell (1985) shows that the non-thermal radio source PKS 0607+17 consists of two regions of

weak ( $T_b \lesssim 1$  K) emission surrounded by a very weak ( $T_b \sim 0.3$  K) extended region of  $\sim 80'$  diameter. No optical filaments are seen on the Palomar red plate (van den Bergh 1978). Arendt (1989) reported the detection of infrared emission near the southern edge.

Figure 3 shows that there is a very weak isolated high-velocity H I emission at the southern portion of the SNR. The large velocity and the positional agreement suggest that the high-velocity H I gas is very likely associated with the SNR.

There is scattered high-velocity H I gas at negative velocities,  $v_{\text{LSR}} < -130$  to  $-10$  km s $^{-1}$ , in this field, but there are no excess emissions coincident with the SNR.

### 5. SUMMARY

We performed a survey of H I emission lines toward all 103 SNRs observable from the Hat Creek Radio Observatory in the catalog of Green (1988). We first made cross scans and divided SNRs into four ranks, where a higher rank means higher probability of an associated H I shell. Twenty SNRs are ranked 3, 25 SNRs are ranked 2, 19 SNRs are ranked 1, and the remaining 39 SNRs are ranked 0. Most rank 3 SNRs are faint ( $T_b < 10$  K at 1.4 GHz) in continuum emission, which seems to be consistent with an idea that the older SNRs are fainter continuum sources. The distribution of rank 2 and rank 3 SNRs in the ( $l, v$ )-plane suggests that the detection of a SNR H I shell is limited by the background emission. We also made  $9 \times 9$  maps at half-beam spacing for all sources ranked 2 or 3 except for G0.9+0.1. We summarize below our main results.

1. Twelve rank 2 sources show an excess emission significantly brighter than the surrounding pixels over a wide ( $> 10$  km s $^{-1}$ ) velocity interval and are very likely to be associated with SNRs. They are G6.4-0.1 (W28), G8.7-0.1 (W30), G11.4-0.1, G12.0-0.1, G32.8-0.1 (Kes 78), G33.6+0.1 (HC 13), G39.2-0.3 (HC 24), G93.7-0.2 (CTB 104A), G189.1+3.0 (IC 443), G349.7+0.2, G352.7-0.1, and G357.7-0.1 (MSH 17-39).

2. In five rank 3 sources, G9.8+0.6, G41.1-0.3 (3C 397), G40.5-0.5, G42.8+0.6, and G65.3+5.7, the high-velocity H I

emission is detected, but it is probably *not* associated with the SNRs.

3. The other 15 rank 3 sources appear to have associated high-velocity H I gas. In two sources, G24.7-0.6 and G49.2-0.7, however, our low-resolution channel maps seem to indicate that the high-velocity gas is associated with a H II region complex very close to the SNR instead of the SNR itself. The relationship between the high-velocity gas, the H II region complexes, and the SNRs needs further study. The expansion velocity and mass of the associated high-velocity H I gas are derived (Table 4). The expansion velocity ranges from 70 to 160 km s $^{-1}$ , and the dynamical ages of the sources range from  $3 \times 10^4$  to  $5 \times 10^5$  yr, with most (80%) of them younger than  $1.2 \times 10^5$  yr. There is no apparent correlation between their physical parameters, which may suggest different physical conditions in an ambient medium for different SNRs.

4. In four rank 3 sources, G24.7-0.6, G49.2-0.7 (W51), G69.0+2.7 (CTB 80), and G89.0+4.7 (HB 21), the H I maps show a velocity structure implying an expanding shell. We obtained the mass distribution  $M(v_\ell)$ , the mass per unit line-of-sight velocity interval  $v_\ell$ , for these sources, and found that it varies as  $M(v_\ell) \propto v_\ell^{-3}$  (Fig. 7). This mass distribution can result either from a systematic density and velocity gradient inside the shell or from clumps with different masses inside the shell. We prefer the latter, because the same trend in all four sources suggests that it has probably resulted from the characteristics of the general interstellar medium, i.e., multi-phase interstellar medium. Also, in the case of CTB 80, the former requires a shell which is much thicker,  $\Delta R/R \gtrsim 0.7$ , than observed.

Most sources need more observations at higher resolution, and our results are preliminary until high-resolution observations are available.

We wish to thank J. Biegging and C. F. McKee for helpful comments. B. C. K. would like to thank the Center for Astrophysics for its hospitality and financial support during a portion of this research. This work has been supported by NSF grant AST-8818544.

### REFERENCES

- Angerhofer, P. E., Becker, R. H., & Kundu, M. R. 1977, *A&A*, 55, 11  
 Arendt, R. G. 1989, *ApJS*, 70, 181  
 Assousa, G. E., & Erkes, J. W. 1973, *AJ*, 78, 885  
 Bertout, C., & Magnan, C. 1987, *A&A*, 183, 319  
 Biegging, J. 1975, in *H II Regions and Related Topics*, ed. T. L. Wilson & D. Downes (Heidelberg: Springer-Verlag), 443  
 Bohigas, J., Ruiz, M. T., Carraso, L., Salas, L., & Herrera, M. A. 1983, *Rev. Mexicana Astr. Af.*, 8, 155  
 Bonsignori-Facondi, S. R., & Tomasi, D. T. 1979, *A&A*, 77, 93  
 Braun, R., & Strom, R. G. 1986, *A&AS*, 63, 345  
 Caswell, J. L. 1985, *AJ*, 90, 1224  
 Chevalier, R. A. 1974, *ApJ*, 188, 501  
 Chevalier, R. A., & Liang, E. P. 1989, *ApJ*, 344, 332  
 Cioffi, D. F., McKee, C. F., & Bertschinger, E. 1989, *ApJ*, 334, 252  
 Colomb, F. R., & Dubner, G. 1980, *A&A*, 82, 244  
 ———. 1982, *A&A*, 112, 141  
 Crampton, D., Georgelin, Y. M., & Georgelin, Y. P. 1978, *A&A*, 66, 1  
 DeNoyer, L. K. 1978, *MNRAS*, 183, 187  
 ———. 1983, *ApJ*, 264, 141  
 Dickel, J. R., & Willis, A. G. 1980, *A&A*, 85, 55  
 D'Odorico, S., & Sabbadin, F. 1977, *A&AS*, 28, 439  
 Downes, A. J. B., Pauls, T., & Salter, C. J. 1986, *MNRAS*, 218, 393  
 Downes, D., Wilson, T. L., Biegging, J., & Wink, J. 1980, *A&AS*, 40, 379  
 Fesen, R. A., Blair, W. P., Kirshner, R. P., Gull, T. R., & Parker, R. A. R. 1981, *ApJ*, 247, 148  
 Fesen, R. A., Shull, J. M., & Saken, J. M. 1988, *Nature*, 334, 229  
 Fich, M., Blitz, L., & Stark, A. A. 1989, *ApJ*, 342, 272  
 Fukui, Y., & Tatematsu, K. 1988, in *IAU Colloquium 101, Supernova Remnants and the Interstellar Medium*, ed. R. S. Roger & T. L. Landecker (Cambridge: Cambridge Univ. Press), 261  
 Giovanelli, R., & Haynes, M. P. 1979, *ApJ*, 230, 404  
 Green, D. A. 1988, *Ap&SS*, 148, 3  
 Hester, J. J., & Kulkarni, S. R. 1988, *ApJ*, 331, L121  
 Higgs, L. A., Landecker, T. L., & Roger, R. S. 1977, *AJ*, 82, 718  
 Hill, I. E. 1974, *MNRAS*, 169, 59  
 Huang, Y.-L., & Thaddeus, P. 1986, *ApJ*, 309, 804  
 Hulsbosch, A. N. M., & Wakker, B. P. 1988, *A&AS*, 75, 191  
 Knapp, G. R., & Kerr, F. J. 1974, *A&A*, 33, 463  
 Koo, B.-C., Reach, W. T., Heiles, C., Fesen, R. A., & Shull, J. M. 1990, *ApJ*, 364, 178  
 Kulkarni, S. R., Clifton, T. R., Backer, D. C., Foster, R. S., Fruchter, A. S., & Taylor, J. H. 1988, *Nature*, 331, 50  
 Kulkarni, S. R., & Fich, M. 1985, *ApJ*, 289, 792  
 Landecker, T. L., Pineault, S., Routledge, D., & Vaneldik, J. F. 1982, *ApJ*, 261, L41  
 Landecker, T. L., Roger, R. S., & Higgs, L. A. 1980, *A&AS*, 39, 133  
 Leahy, D. A. 1987, *MNRAS*, 228, 907  
 Lozinskaya, T. A. 1979, *Australian J. Phys.*, 32, 113  
 ———. 1981, *Soviet Astr. Letters*, 7, 17  
 Lozinskaya, T. A., & Sitnik, T. G. 1977, *Soviet Astr.*, 21, 456  
 ———. 1979, *Soviet Astr. Letters*, 5, 186  
 McKee, C. F. 1988, in *IAU Colloquium 101, Supernova Remnants and the Interstellar Medium*, ed. R. S. Roger & T. L. Landecker (Cambridge: Cambridge Univ. Press), 473

- McKee, C. F., Cowie, L. L., & Ostriker, J. P. 1978, *ApJ*, 219, L23  
McKee, C. F., & Ostriker, J. P. 1977, *ApJ*, 217, 148  
McKee, C. F., Van Buren, D., & Lazareff, B. 1984, *ApJ*, 278, L115  
Milne, D. K. 1979, *Australian J. Phys.*, 32, 83  
Pineault, S., Landecker, T. L., & Routledge, D. 1987, *ApJ*, 315, 580  
Pineault, S., Pritchett, C. J., Landecker, T. L., Routledge, D., & Vaneldik, J. F. 1985, *A&A*, 151, 52  
Reich, W., Fürst, E., Steffen, P., Reif, K., & Haslam, C. G. T. 1984, *A&AS*, 58, 197  
Reich, W., Reich, P., & Fürst, E. 1990, *A&AS*, 83, 539  
Reynolds, S. P. 1988, in *Galactic and Extragalactic Astronomy*, ed. G. L. Verschuur & K. I. Kellermann (New York: Springer-Verlag), 439  
Romney, J. D., Schilizzi, R. T., Fejes, I., & Spencer, R. E. 1987, *ApJ*, 321, 822  
Routledge, D., Landecker, T. L., & Vaneldik, J. F. 1986, *MNRAS*, 221, 809  
Sato, F. 1973, *PASJ*, 25, 135  
———. 1974, *PASJ*, 26, 459  
Shull, J. M. 1987, in *Interstellar Processes*, ed. D. J. Hollenbach & H. A. Thronson, Jr. (Dordrecht: Reidel), 225  
Sieber, W., Haslam, C. G. T., & Salter, C. J. 1979, *A&A*, 74, 361  
Smith, A., Jones, L. R., Watson, M. G., Willingale, R., & Seward, F. D. 1985, *MNRAS*, 217, 99  
Spitzer, L. I. 1978, *Physical Processes in the Interstellar Medium* (New York: Wiley-Interscience)  
Tatematsu, K., Fukui, Y., Landecker, T. L., & Roger, R. S. 1990, *A&A*, 237, 189  
Tenorio-Tagle, G., Bodenheimer, P., Franco, J., & Różyczka, M. 1990, *MNRAS*, 244, 563  
van den Bergh, S. 1978, *ApJS*, 38, 119  
———. 1980, *ApJ*, 236, L23  
van der Laan, H. 1962, *MNRAS*, 124, 125  
Willis, A. G. 1973, *A&A*, 26, 237  
Woltjer, L. 1972, *ARA&A*, 10, 129  
Wootten, H. A. 1977, *ApJ*, 216, 440